The Structure of Massive Star-Forming Galaxies from JWST and ALMA: Dusty, High Redshift Disk Galaxies

Steven Gillman,[1,2]* Ian Smail,[3] Bitten Gullberg,[1,2] A. M. Swinbank,[3] Aswin P. Vijayan,[1,2,4] Minju Lee,[1,2] Gabe Brammer,[1,5] U. Dudzevičiūtė,[6] Thomas R. Greve,[1,2,7] Omar Almaini,[8] Malte Brinch,[1,2] Scott C. Chapman,[9] Chian-Chou Chen,[10] Soh Ikarashi,[11,12,13] Yuichi Matsuda,[11,14,15] Wei-Hao Wang,[10] Fabian Walter,[5,16] and Paul P. van der Werf[17]

[1] Cosmic Dawn Center (DAWN), Denmark
   e-mail: srigi@space.dtu.dk
[2] DTU-Space, Elektrovej, Building 328 , 2800, Kgs. Lyngby, Denmark
[3] Centre for Extragalactic Astronomy, Department of Physics, Durham University, South Road, Durham DH1 3LE, UK
[4] Astronomy Centre, University of Sussex, Falmer, Brighton BN1 9QH, UK
[5] Niels Bohr Institute, University of Copenhagen, Jagtvej 128, DK-2200 Copenhagen N, Denmark
[6] Max-Planck-Institut für Astronomie, Königstuhl 17, 69117 Heidelberg, Germany
[7] Dept. of Physics and Astronomy, University College London, Gower Street, London WC1E 6BT, United Kingdom
[8] School of Physics and Astronomy, University of Nottingham, Nottingham NG7 2RD, UK
[9] Dept of physics, Dalhousie University, Halifax NS, Canada
[10] Academia Sinica Institute of Astronomy and Astrophysics (ASIAA), No. 1, Section 4, Roosevelt Road, Taipei 10617
[11] National Astronomical Observatory of Japan, 2-21-1 Osawa, Mitaka, Tokyo, 181-8588, Japan
[12] Junior College, Fukuoka Institute of Technology, 3-30-1 Wajiro-higashi, Higashi-ku, Fukuoka, 811-0295 Japan
[13] Department of Physics, General Studies, College of Engineering, Nihon University, 1 Nakagawara, Tokusada, Tamuramachi, Koriyama, Fukushima, 963-8642, Japan
[14] Graduate University for Advanced Studies (SOKENDAI), Osawa 2-21-1, Mitaka, Tokyo 181-8588, Japan
[15] Cahill Center for Astronomy and Astrophysics, California Institute of Technology, MS 249-17, Pasadena, CA 91125, USA
[16] National Radio Astronomy Observatory, Pete V. Domenici Array Science Center, P.O. Box O, Socorro, NM 87801, USA
[17] Leiden Observatory, Leiden University, P.O. Box 9513, 2300 RA Leiden, The Netherlands

June 7th 2024

ABSTRACT

We present an analysis of the JWST NIRCam and MIRI morphological and structural properties of 80 massive $(\log_{10}(M_*[M_\odot]) = 11.2 \pm 0.1)$ dusty star-forming galaxies at $z = 2.7^{+1.2}_{-0.7}$, identified as sub-millimetre galaxies (SMGs) by ALMA, that have been observed as part of the JWST PRIMER project. To compare the structure of these massive, active galaxies to more typical star-forming galaxies, we define a sample of 850 field galaxies with matched redshifts and specific star formation rates. From visual classification of the dusty star-forming galaxies, we identify $20 \pm 5\%$ as candidate late-stage major mergers, a further $40 \pm 10\%$ as potential minor mergers and $40 \pm 10\%$ which have comparatively undisturbed disk-like morphologies, with no obvious massive neighbours on $\lesssim 20 - 30$ kpc (projected) scales. These rates are comparable to those for the field sample and indicate that the majority of the sub-millimetre-detected galaxies are not late-stage major mergers, but have interaction rates similar to the less-active and less massive field population at $z \sim 2$–3. Through a multi-wavelength morphological analysis, using parametric and non-parametric techniques, we establish that SMGs have comparable near-infrared, mass normalised, sizes to the less active population, $R_{50}^{\mathrm{F444W}} = 2.7 \pm 0.2$ kpc versus $R_{50}^{\mathrm{F444W}} = 3.1 \pm 0.1$ kpc, but exhibit lower Sérsic indices, consistent with bulge-less disks: $n_{\mathrm{F444W}} = 1.1 \pm 0.1$, compared to $n_{\mathrm{F444W}} = 1.9 \pm 0.1$ for the less active field. The SMGs exhibit greater single-Sérsic fit residuals and their morphologies are more structured at 2μm relative to 4μm when compared to the field galaxies. This appears to be caused by significant structured dust content in the SMGs and we find evidence for dust reddening as the origin of the morphological differences by identifying a strong correlation between the F200W−F444W pixel colour and the 870μm surface brightness using high-resolution ALMA observations. We conclude that SMGs and less massive and less actively star-forming galaxies at the same epochs share a common disk-like structure, but the weaker bulge components (and potentially lower black hole masses) of the SMGs results in a lower dynamical stability. Consequently, instabilities triggered either secularly or generally by minor external perturbations result in higher levels of activity (and dust content) in SMGs compared to typical star-forming galaxies.

Key words. Galaxies: high-redshift – Galaxies: structure – Galaxies: evolution – Sub-millimetre: galaxies

1. Introduction

The relative proportions of highly-dust-obscured and less-obscured star formation appears to vary over the history of the Universe, with the dust-obscured component dominating in galaxy populations at $z \sim 4$–5 down to the present day (e.g., Dunlop et al. 2017; Bouwens et al. 2020; Long et al. 2023). The cause of this transition in star-formation mode may reflect the growing metallicity of the interstellar medium (ISM) in galaxies, less effi-

---

* ORCIDs listed on final page

cient removal of dust from deeper potential wells or structural or geometrical changes in the star-forming regions within galaxies.

The most extreme examples at high redshifts of systems dominated by dust-obscured star formation are the sub-millimetre galaxies (SMGs) with dust masses of $M_d \sim 10^{8-9}$ M$_\odot$ and far-infrared luminosities of $L_{IR} \sim 10^{12-13}$ L$_\odot$ (e.g., Magnelli et al. 2012; Rowlands et al. 2014; Miettinen et al. 2017b; Dudzevičiūtė et al. 2020), placing them into the Ultra or Hyperluminous Infrared Galaxies (U/HyLIRGs), see Hodge & da Cunha (2020) for a full review. Most of these galaxies show high star-formation rates, SFR $\sim 10^{2-3}$ M$_\odot$ yr^{-1};(Swinbank et al. 2014), and correspondingly short gas consumption timescales (e.g., Greve et al. 2005; Miettinen et al. 2017a; Tacconi et al. 2018; Birkin et al. 2021), suggesting that they represent relatively short-lived starbursts, $\lesssim 100$ Myrs, which will result in massive systems with stellar masses of $M_* \sim 10^{11}$ M$_\odot$ (e.g., Wardlow et al. 2011; Simpson et al. 2014; Miettinen et al. 2017a; Dudzevičiūtė et al. 2020).

The high star formation rates and large stellar masses of SMGs have proved challenging to reproduce in theoretical galaxy formation models (e.g., Baugh et al. 2005; Swinbank et al. 2008; Hayward et al. 2013; McAlpine et al. 2019), although more recent attempts have been more successful (e.g., Lower et al. 2023; Cochrane et al. 2023). The models suggest that the high star formation rates in this population are driven by a mix of secular instabilities in gas-rich disks and dynamical triggers due to minor and major mergers (e.g., McAlpine et al. 2019). However, attempts to observationally test these claims using the available rest-frame ultra-violet (UV) Hubble Space Telescope (HST) imaging of $z \sim 1-3$ SMGs were challenging (e.g., Chapman et al. 2003). While the galaxies frequently exhibited irregular morphologies with apparently multiple components (e.g., Swinbank et al. 2010; Chen et al. 2015; Gómez-Guijarro et al. 2018; Zavala et al. 2018; Cowie et al. 2018; Lang et al. 2019; Ling & Yan 2022), their significant dust attenuation ($A_V \gtrsim 2-6$, e.g., Dudzevičiūtė et al. 2020) means that assessing the intrinsic stellar mass morphology of the galaxies from these data was incredibly challenging – especially for the subset of the population that is undetectable in the near-infrared ("NIR-faint" SMGs, Simpson et al. 2014; Dudzevičiūtė et al. 2020; Smail et al. 2021; Ikarashi et al. 2022; Kokorev et al. 2023). Detecting and resolving rest-frame near-infrared emission of SMGs, which is much less affected by dust attenuation and reflects the bulk of the stellar population, is essential to robustly constrain the morphology of their stellar mass. However, this has been beyond the reach of previous instrumentation such as the Infrared Array Camera (IRAC; Fazio et al. 2004) on the Spitzer Space Telescope, which, whilst providing the required near-infrared wavelength coverage from $3.6-8\mu$m, lacked the spatial (sub-arcsecond) resolution required to constrain the underlying morphologies of the stellar emission in SMGs.

However, some progress has been made on understanding the structure of SMGs using high-resolution observations of the dust continuum and gas kinematics in SMGs (e.g., Simpson et al. 2015; Ikarashi et al. 2015; Fujimoto et al. 2017). Thus FWHM $\sim 0\rlap{.}''1-0\rlap{.}''2$ sub-millimetre mapping with ALMA has revealed compact disk-like dust continuum emission arises from compact disk-like structures (i.e., $R_e \sim 1-2$ kpc, Sérsic $n \approx 1$), which are roughly half the size of the galaxy extent in HST H-band imaging (Hodge et al. 2016; Gullberg et al. 2019; Chen et al. 2020; Cochrane et al. 2021). At the highest resolutions, FWHM $\sim 0\rlap{.}''05$, Hodge et al. (2019) identified potential arms and bar-like structures in the dust continuum emission from a small sample of high-redshift SMGs. Resolved kinematic stud-

ies using molecular and atomic fine structure emission lines in the rest-frame far-infrared and sub-/millimetre have uncovered disk-like kinematics for at least a significant fraction of the population (e.g., Hodge et al. 2012; Chen et al. 2017; Lelli et al. 2021; Rizzo et al. 2021; Amvrosiadis et al. 2023). With the advent of the James Webb Space Telescope (JWST, Gardner et al. 2023), high-resolution observations from from the near (1μm) to the mid-infrared (25μm) are now feasible, enabling the infrared emission from counterparts of sub-millimetre bright galaxies to be detected and the issue of their stellar morphology and structures to be finally quantified. Initial morphological studies with JWST have found size evolution with wavelength in sub-millimetre galaxies and less active colour-selected populations at $z \sim 2$ (Chen et al. 2022; Cheng et al. 2023; Suess et al. 2022), with a reduction in half-light radius when observed in the rest-frame near-infrared compared to the rest-frame optical/UV as previously studied with HST. A number of studies have subsequently expanded the samples with JWST and ALMA coverage, confirming that SMGs become more compact (higher concentration, smaller size) at longer wavelengths (e.g. Price et al. 2023; Cheng et al. 2023; Gillman et al. 2023) with the potential impact of dust on the observed morphology becomingly less evident at longer wavelengths (Kokorev et al. 2022; Wu et al. 2023; Kamieneski et al. 2023; Sun et al. 2024). There are also claims of frequent stellar bars in many high-redshift star-forming galaxies (Guo et al. 2023), including examples in SMGs (Smail et al. 2023). However, all of these studies suffer from modest sample statistics, limiting the interpretations of their findings.

In this paper, we present an analysis of the structural properties of a statistically robust sample of ALMA-detected, sub-millimetre detected galaxies that have been observed with JWST NIRCam and MIRI. In Section 2 we define the sample of SMGs that we use in our analysis whilst in Section 3 we present the observations, data reduction and analysis undertaken on the multi-wavelength imaging of these systems (and a matched control sample of less active galaxies selected from the field). In Section 4 we discuss the results from our analysis before summarising our main conclusions in Section 5. Throughout the paper, we assume a ΛCDM cosmology with $\Omega_m = 0.3$, $\Omega_\Lambda = 0.7$, and $H_0 = 70$ km s^{-1} Mpc^{-1}. All quoted magnitudes are on the AB system and stellar masses are calculated assuming a Chabrier initial mass function (IMF) (Chabrier 2003).

2. Sample Selection

To build a sample of ALMA-detected SMGs with near-infrared JWST coverage, we utilise the AS2UDS (Stach et al. 2019) and AS2COSMOS (Simpson et al. 2020) surveys as our parent sample. The AS2UDS and AS2COSMOS surveys are ALMA 870μm follow-up programs of 716 and 180 850μm SCUBA-2 sources that are detected at $> 4\sigma$ in the S2CLS (Geach et al. 2017) map of the UKIDSS Ultra-Deep Survey (UDS; Lawrence et al. 2007) and the S2COSMOS (Simpson et al. 2019) map of the Cosmic Evolution Survey (COSMOS; Scoville et al. 2007) respectively. These two surveys provide an initial candidate sample of 896 SMGs with precise ALMA identifications, selected at SNR $\gtrsim 4$, for which we can use to characterise their near-infrared JWST counterparts.

We cross-match the ALMA positions for the SMGs as presented in Stach et al. (2019) for AS2UDS and Simpson et al. (2020) for AS2COSMOS, with the footprint of the JWST/NIRCam and JWST/MIRI observations from The Public Release IMaging for Extragalactic Research (PRIMER; Dunlop et al. 2021) survey. PRIMER is a multi-band, multi-instrument
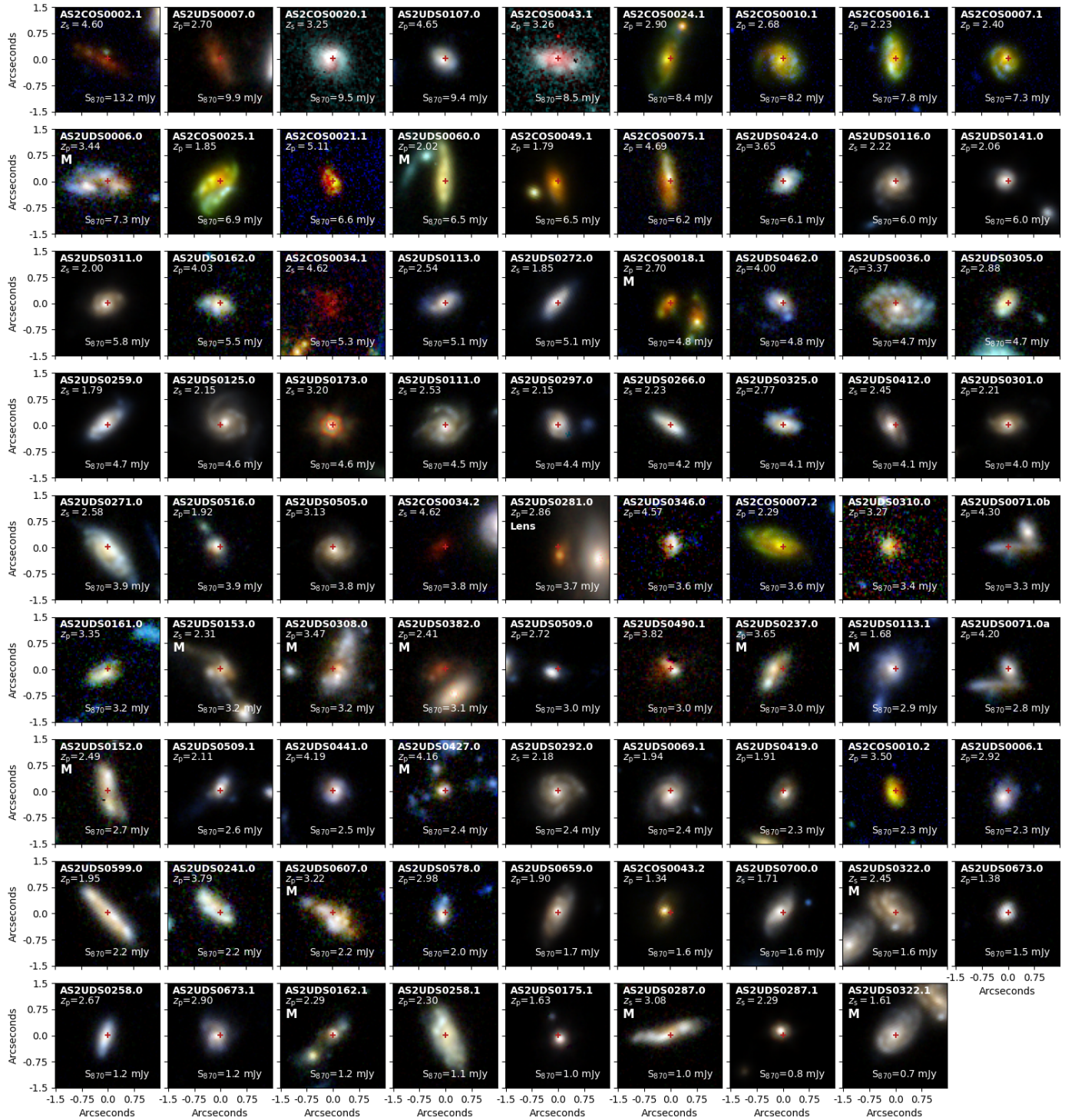
Fig. 1: The combined AS2UDS and AS2COSMOS SMG sample in the PRIMER survey ranked in descending ALMA 870μm flux. For each SMG we show the $3''0 \times 3''0$ false colour image (F444W/F356W/F277W as R/G/B), labelling the SMG ID, redshift (MAGPHYS derived, z_p, or spectroscopic, z_s) and ALMA 870μm flux density. We further label the SMGs visually classified as major mergers (M) or affected by gravitational lensing (Lens). The red cross indicates the ALMA 870μm position.

survey of UDS and COSMOS covering 234 and 144 sq. arcmin respectively. The observations consist of the seven wide-band and one medium-band NIRCam filter (F090W, F115W, F150W, F200W, F277W, F356W, F410M, F444W) as well as two wide-band MIRI filters (F770W, F1800W). Parts of the UDS and COSMOS fields also benefit from HST ACS and WFC3 cover-

age from CANDELS (Grogin et al. 2011) sampling the observed frame optical (0.4μm) to near-infrared (1.6μm).

For our analysis, we require the SMGs to be covered by the JWST/NIRCam long-wavelength filter F444W ensuring that the observed-frame near-infrared is sampled. This results in a sample of 66 AS2UDS and 22 AS2COSMOS SMGs. A summary of

the ALMA properties and HST and JWST coverage is presented in Appendix A. Of the 88 SMGs, 12 have no HST coverage. Two SMGs have JWST imaging in only three bands (F444W, F277W, F200W) while the other 86 SMGs are covered by three or more JWST bands, with 37 SMGs having the maximum ten available JWST filters covering from 0.9 to 18 μm.

The 88 SMGs have a median ALMA 870μm flux of $S_{870\mu m} = 3.8 \pm 0.4$ mJy, with a 16th to 84th percentile range of $S_{870\mu m} = 1.8 - 6.1$ mJy. The SMGs sample the faint end of the full AS2COSMOS and AS2UDS $S_{870\mu m}$ distribution with ranges from $S_{870\mu m} = 0.7 - 19.2$ mJy and $S_{870\mu m} = 0.6 - 13.6$ mJy respectively. Majority of the AS2UDS SMGs (51/66) were observed with ALMA at resolutions of $\simeq 0\rlap{.}''3$ FWHM as presented in Stach et al. (2019). The remaining 15 SMGs in UDS were observed at high-resolution $\simeq 0\rlap{.}''2$ FWHM (Gullberg et al. 2019). The ALMA maps of the 22 SMGs in the COSMOS field were tapered to a resolution of $0\rlap{.}''8$ FWHM (Simpson et al. 2020).

3. Reduction & Analysis

In this section, we present our reduction, analysis and compilation of the photometric data that we use to characterise the multi-wavelength properties of the SMGs.

3.1. JWST & HST

We homogeneously process the JWST NIRCam and MIRI observations, retrieving the level-2 data products (version = jwst_1069.pmap) from the STScI website[1] and processing them with the GRIZLI pipeline (Brammer & Matharu 2021; Brammer et al. 2022)[2]. For the NIRCam data, additional steps were employed to deal with diagonal striping seen in some exposures, cosmic rays and stray light. Whilst for the MIRI exposures time-dependent sky flats are applied in an approach similar to recent JWST studies (e.g., Yang et al. 2023). We further incorporate the available optical and near-infrared data available in the Complete Hubble Archive for Galaxy Evolution (CHArGE, Kokorev et al. 2022), providing multiband observed-frame imaging from 0.4 to 1.6μm for a subset of the sources. We align all the imaging to Gaia DR3 (Gaia Collaboration et al. 2021), co-add, and drizzle the final mosaics to a $0\rlap{.}''04$ pixel scale (Fruchter & Hook 2002) for all JWST and HST filters.

3.2. Photometry

For JWST and HST bands we extract sources using SEP (Barbary et al. 2016), a python version of SOURCE EXTRACTOR (Bertin & Arnouts 1996a), with a noise-weighted combined F277W+F356W+F444W NIRCam image as the detection image. For each source we make a cutout in each of the HST and JWST bands, centred on this NIRCam long-wavelength detected source. Three arcsecond colour images made from the F444W/F356W/F277W NIRCam bands for the SMGs are shown in Figure 1. Aperture photometry is performed in elliptical apertures with a minimum diameter of $1\rlap{.}''0$ and corrected to the "total" values following Kron (1980). The aperture corrections are computed on the NIRCam LW stacked image and applied to all bands. The MIRI observations were processed prior to the release of the updated photometric calibrations. We thus scale

the measured flux in the F770W and F1800W bands by 0.85 and 1.03 respectively following the JWST documentation. We determine a median F444W AB magnitude for the SMG sample of $m_{F444W} = 21.7 \pm 0.3$ with a $16^{th} - 84^{th}$ percentile range of $m_{F444W} = 20.3 - 23.1$.

We compile the mid-infrared to radio (5.8μm to 1.4GHz) photometry for our sources from Dudzevičiūtė et al. (2020) and Simpson et al. (2020). For the SMGs with no MIRI F770W and F1800W imaging, we adopt the IRAC channel 3 (5.8μm) and channel 4 (8μm) photometry, if IRAC channel 1 (3.6μm) flux is within 10 percent of the NIRCam F356W and IRAC channel 2 (4.5μm) flux is within 10 percent of the NIRCam F444W. We employ the IRAC photometry for two out of seven AS2COSMOS SMGs without MIRI coverage and 11 out of 38 AS2UDS SMGs.

3.3. Final Sample

Having collated a sample of 88 AS2UDS and AS2COSMOS SMGs lying within the JWST PRIMER fields, we visually inspect each of the galaxies' JWST imaging to verify the association of the near-infrared counterpart to the ALMA source. Of the 88 SMGs, we identify one SMG, AS2UDS0490.0, with no clear NIRCam counterpart, with a F444W magnitude of $m_{F444W} = 26.7 \pm 0.6$ detected at 1.4σ. There is no MIRI coverage or any detection of this $S_{870} = 2.7$ mJy (SNR = 4.5) source between UV and radio, thus we conclude it is likely spurious, with the ALMA catalogue of 707 sources from Stach et al. (2019) expected to have a two percent spurious fraction, and so exclude the source from our sample. We also remove two SMGs, AS2COS0005.1 and AS2COS0005.2, which appear gravitational lensed and thus the derivation of their intrinsic properties including morphology would require detailed and uncertain lens modelling (e.g. Amvrosiadis et al. 2018; Bendo et al. 2023; Pearson et al. 2024). We remove three UDS sources (AS2UDS0106.0, AS2UDS0175.0 and, AS2UDS0069.0) and three COSMOS sources (AS2COS0017.1, AS2COS0032.1 and, AS2COS0035.1) due to partial coverage in the JWST NIRCam imaging. Finally, one ALMA source, AS2UDS00071.0, is deblended in the NIRCam F444W imaging, and high-resolution ALMA observations (Gullberg et al. 2019), into two sources which we label AS2UDS00071.0a and AS2UDS00071.0b. We model the morphology of AS2UDS0071.0a and AS2UDS0071.0b independently and scale the blended photometry by the flux ratio of the two sources. Thus in the final sample, we have 80 SMGs, for which the HST and JWST coverage for each SMG is detailed in Appendix A.

3.4. SED Fitting

Having defined a final sample of 80 SMGs with robust near-infrared counterparts, we use the SED fitting code Multiwavelength Analysis of Galaxy Physical Properties and Photometric Redshift (MAGPHYS+PHOTO-z, hereafter referred to as MAGPHYS; da Cunha et al. 2015; Battisti et al. 2019), to derive the physical properties of each SMG[3]. For 22 of the SMGs spectroscopic redshifts are available from the literature and ongoing millimetre and near-infrared spectroscopic surveys (e.g., McLure et al. 2018; Mitsuhashi et al. 2021). For these sources we

---

[3] We note that we do not include an AGN component in the MAGPHYS modelling as the fraction with AGN contributions is expected to be small (e.g., Stach et al. 2019)
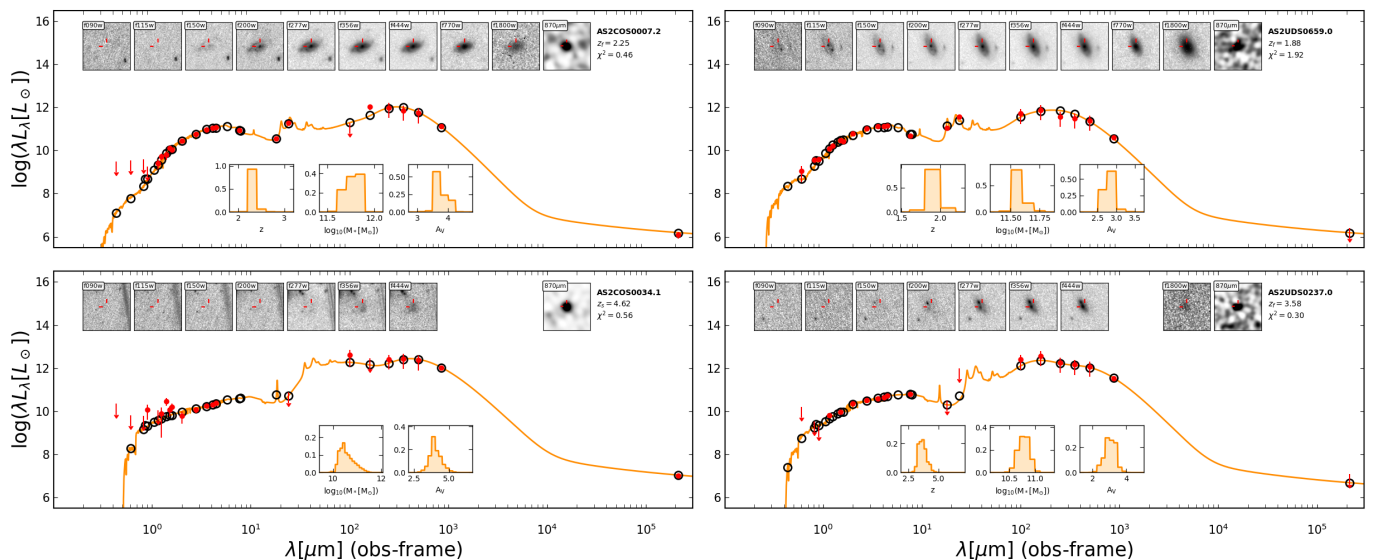
Fig. 2: The multi-wavelength SEDs for four example SMGs (AS2UDS0301.0, AS2UDS0346.0, AS2COS0002.1 and AS2UDS0237.0) that demonstrate the range of observed-frame infrared colours displayed by the SMG sample. For each source, we indicate the observed flux and error in each band with a red circle and errorbar. Arrows show upper limits at 3σ for wavelengths below 10μm and 1σ for wavelengths beyond 10μm. We over plot the best-fit MAGPHYS derived SED (orange line) and model fluxes (black circles). Below each SED we display probability distributions of the MAGPHYS derived properties (redshift (unless spectroscopic), stellar mass and A_V) and report the best-fit redshift and reduced chi-square at the top right. Above the SED we display the multi-wavelength JWST and ALMA 870μm imaging used as part of the analysis, with the SMG centroid indicated by the red tick markers. Appendix B shows the SEDS for the full sample.

use the high-redshift version of MAGPHYS, (MAGPHYS+HIGHz (v2); da Cunha et al. 2015; Battisti et al. 2019) with the redshift fixed to the spectroscopic redshift of each source, as detailed in Appendix A.

MAGPHYS is a physically motivated SED fitting code that utilises the energy balance technique to fit the multi-wavelength photometry from UV to radio. This approach, as tested on SMGs by da Cunha et al. (2015) and Dudzevičiūtė et al. (2020), and simulated galaxies (e.g., Dudzevičiūtė et al. 2020; Haskell et al. 2023), models the sub-millimetre and optical emission as originating from the same region of the galaxy. For a discussion of using the MAGPHYS SED code to model high redshift SMGs, we refer the reader to Dudzevičiūtė et al. (2020). For consistencies with Dudzevičiūtė et al. (2020), for non-detections at wavelengths shorter than 8μm, we adopt a flux and uncertainty of $0\pm3\sigma$ while for those beyond 10μm, we use $1.5\pm1.0\sigma$.

In Figure 2, we show examples of the multi-wavelength photometry and MAGPHYS SED fits, with the fits for the whole sample presented in Appendix B. We summarise some of the key derived physical properties of the SMG sample in Figure 3. We estimate a median redshift of $z = 2.7 \pm 0.15$ with a (16$^{\text{th}}$ to 84$^{\text{th}}$ percentile range of $z = 1.9 - 3.9$, which is comparable to that derived by Dudzevičiūtė et al. (2020) for AS2UDS $z = 2.6 \pm 0.8$ and the median redshift of the AS2COSMOS survey ($z = 2.7 \pm 0.9$) as derived by Simpson et al. (2020), as well as other studies of SMGs (e.g., da Cunha et al. 2015; Ling & Yan 2022). From the MAGPHYS SED fitting, we derive a median stellar mass for the SMGs of $\log_{10}(M_*[M_\odot]) = 11.20 \pm 0.10$ with a 16$^{\text{th}} - 84^{\text{th}}$ percentile range of $\log_{10}(M_*[M_\odot]) = 10.6 - 11.6$, and a median specific star-formation rate of $\log_{10}(\text{sSFR}[\text{yr}^{-1}]) = -8.7 \pm 0.1$ with a 16$^{\text{th}} - 84^{\text{th}}$ percentile range of $\log_{10}(\text{sSFR}[\text{yr}^{-1}]) = -9.2$ to -8.0. We derive a median dust mass of $\log_{10}(M_d[M_\odot]) = 8.8 \pm 0.1$ with a 16$^{\text{th}} - 84^{\text{th}}$ percentile range of $\log_{10}(M_d[M_\odot]) = 8.4 - 9.1$ and a median infrared luminosity of $\log_{10}(L_{IR}[L_\odot]) = 12.6 \pm 0.1$

with a 16$^{\text{th}} - 84^{\text{th}}$ percentile range of $\log_{10}(L_{IR}[L_\odot]) = 12.3 - 12.8$. These are consistent with the parent sample of 707 SMGs in AS2UDS, for which Dudzevičiūtė et al. (2020) derived a median stellar and dust mass of $\log_{10}(M_*[M_\odot]) = 11.1^{+0.2}_{-0.3}$ and $\log_{10}(M_d[M_\odot]) = 8.8^{+0.4}_{-0.4}$ and a median specific star-formation rate and infrared luminosity of $\log_{10}(\text{sSFR}[\text{yr}^{-1}]) = -8.73 \pm 0.04$ and $\log_{10}(L_{IR}[L_\odot]) = 12.45 \pm 0.02$

As expected given the JWST photometry agrees with earlier IRAC and HST or ground-based observations, while typically being more sensitive, the basic derived properties of the SMGs don't alter when JWST photometry is included. The main benefit of deeper observations at $1 - 3$μm is improved constraints on the presence Balmer breaks at $z \sim 1 - 6$.

3.5. Field Sample

To investigate the physical mechanism that drives and differentiates our SMG sample from the typical star-forming population at the same epochs $z = 2 - 5$, we compare their multi-wavelength properties to a sample of less active field galaxies which we construct from the K-band selected sample analysed by Dudzevičiūtė et al. (2020) in the UKIDSS UDS field for which deep 22-band photometry is available covering the UV/optical through to the far-infrared/submillimeter and radio. Dudzevičiūtė et al. (2020) used the MAGPHYS code to derive photometric redshifts, stellar masses and other physical properties for the $\sim 300,000$ $K_{AB} \leq 25.7$ galaxies in this ~ 0.8 degree^2 field from the UKIDSS survey (Almaini in prep.). Starting from this field catalogue we select galaxies with no photometric flags that lie within the footprint of the JWST PRIMER survey and have estimated dust masses and far-infrared luminosities that ensure they are less actively star-forming than our SMG sample: $M_{dust} = 10^7 - 10^8$ M$_\odot$ and $L_{IR} = 10^{11} - 10^{12}$ L$_\odot$. We then bin the redshift distribution of the SMGs and field galaxies in $\Delta z = 0.5$ bins and in each
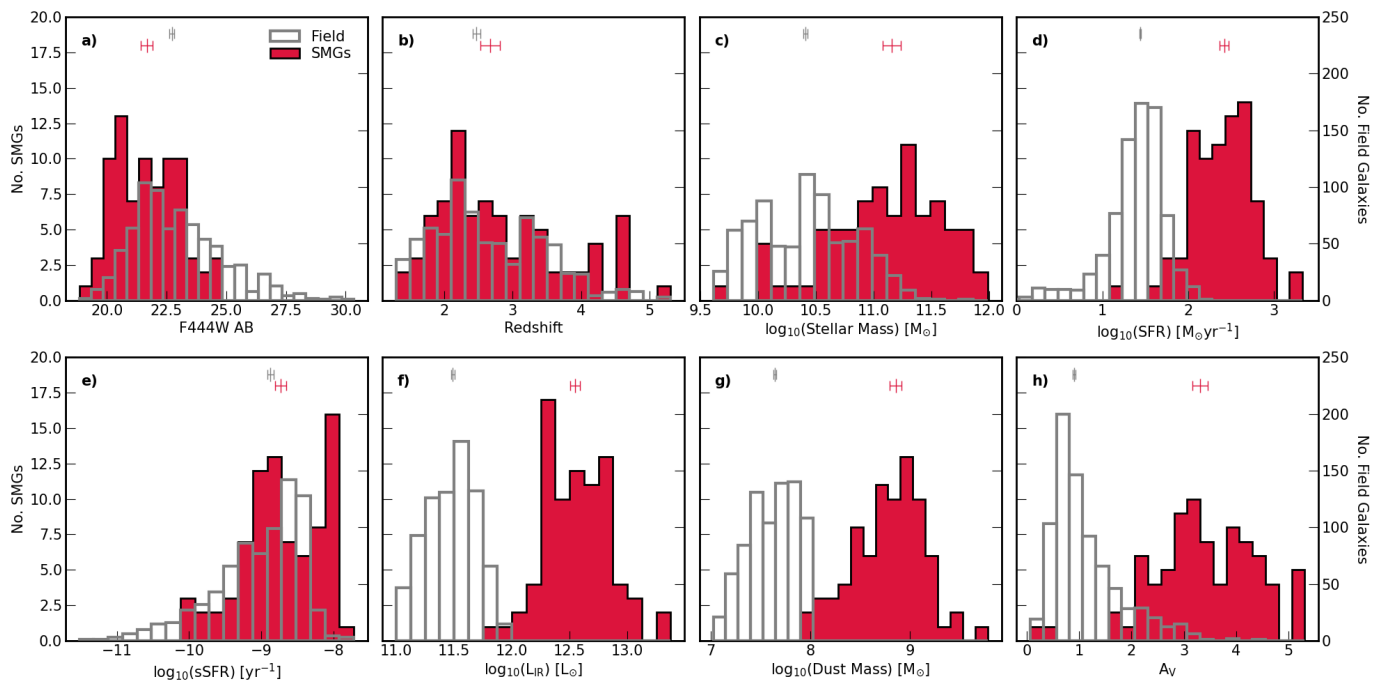
Fig. 3: Distributions of the MAGPHYS derived SED properties for the SMG sample (*red*) and field sample *(open grey histograms)*. We show the F444W AB magnitude *(a)*, photometric redshift *(b)*, stellar mass *(c)*, star formation rate *(d)*, specific star formation rate *(e)*, infrared luminosity *(f)*, dust mass *(g)* and *V*-band attenuation (A$_V$) *(h)*. For each distribution, we indicate the bootstrapped median and uncertainty for SMGs (*red marker and errorbar*) and the matched field sample (*grey marker and errorbar*). By construction, the field sample mirrors the SMG sample in redshift and specific star-formation rate distributions while having significantly lower dust masses, infrared luminosity and star-formation rates. The resulting field sample exhibits much lower A$_V$ than the SMGs.

bin we rank the field galaxies based on their stellar masses. We then determine the number of SMGs for each bin and select ten times as many field galaxies from the corresponding redshift bin, starting with the most massive and going down the stellar-mass ranked list. In this way, we construct a control sample that accurately matches the redshift distribution of our SMG sample and comprises the most massive galaxies at each epoch that have dust masses and far-infrared luminosities below those determined for the SMG population. We adopt the photometry and MAGPHYS SED fitting results from Dudzevičiūtė et al. (2020). In Figure 3, we show the distribution of physical properties for the UDS field sample in comparison to the SMGs. By construction, the field sample has similar redshift and specific star-formation rates to the SMG sample, whilst having significantly lower dust masses and A$_V$. The field sample has a median redshift and median absolute deviation of $z = 2.5 \pm 0.1$, whilst their specific star-formation rates are sSFR $= -8.88 \pm 0.04$ yr^{-1} and A$_V = 0.90 \pm 0.03$. The field sample is fainter in F444W magnitude with a median value of $m_{\text{F444W}} = 22.74 \pm 0.10$ compared to $m_{\text{F444W}} = 21.70 \pm 0.30$, which is reflected in the distributions of stellar mass.

3.6. Morphological Analysis

In Figure 1 we show NIRCam F277W/F356W/F444W colour images of the SMGs, highlighting the diverse range of rest-frame optical – near-infrared morphologies from faint and red galaxies, interacting and merging systems to disks and grand-design spirals. These near-infrared observations sample the galaxy population at $\leq 1\mu$m in the rest frame at ≈ 1 kpc resolution and thus provide insights into the structure and morphology of the stellar

continuum emission which are much less affected by dust than previously possible.

We first visually assess the morphologies of the SMGs and the field sample. In addition, to quantify the rest-frame near-infrared morphology of the SMGs and field galaxies, we employ both a non-parametric and parametric analysis of the JWST observations. We exclude the HST observations from our morphological analysis because at the median redshift of our sample ($z \sim 2.7$), HST observations are sensitive to the rest-frame UV/optical emission of the galaxies where SMGs are inherently faint. The longer wavelength HST observations sampling the observed frame 1.6μm emission is also well covered by higher signal to noise JWST observations.

The parametric and non-parametric analysis of the JWST imaging employs $4\overset{''}{.}0 \times 4\overset{''}{.}0$ cutouts of each source with pixel scales of $0\overset{''}{.}04$ per pixel. The cutout in each filter is centred on the source detection in NIRCam long-wavelength (F277W+F356W+F444W) stacked image, as detailed in Section 3.2. We first smooth the source segmentation map generated from SEP (see Section 3.2) using the binary dilation routine in PHOTUTILS (Bradley et al. 2022). Then, excluding this segmented region, we mask the remaining sources in the cutout, down to a 1σ isophote. This ensures full masking of any contaminants (spurious or otherwise). We further use PHOTUTILS to model (and remove) the background level in each cutout as well as to quantify the root-mean-square (rms) noise. In the following sections "cutout" refers to these $4\overset{''}{.}0 \times 4\overset{''}{.}0$, background subtracted and masked image that is used in the morphological analysis that follows.

Prior to measuring the morphology of the galaxies we first derive the point spread function (PSF) for each of the JWST

bands. We use WEBBPSF (version 1.2.1; Perrin et al. 2014) to generate PSF models for the MIRI and NIRCam detectors (for both short- and long-wavelength channels) which are calibrated with wavefront models at the epoch of the observations. The PSFs for each NIRCam and MIRI filter are then inserted into individual exposures of the final mosaic and drizzled to the final world coordinate system solution, producing a field of view averaged PSF model.

3.6.1. Visual Morphology

We undertake a crude initial assessment of the visual morphology of the SMGs compared to a similar subset of the field sample. This involved interactive inspection of both the colour images and GALFIT residual maps in the F444W band (Figure 1 & 5) of the ALMA counterpart to identify distorted morphologies, asymmetric structures or potential tidal features. In addition, we assessed the presence of companions (either within ∼1 mag in brightness of the target galaxy, or fainter) within a wider $10''.0 \times 10''.0$ region (out to a radius of ∼30kpc). Strongly disturbed galaxies, those with tidal features or disturbed galaxies with bright companions were classed as "major" mergers (these are marked in Figure 1), while less disturbed galaxies or those with asymmetries and fainter companions were classed as potential "minor" mergers.

3.6.2. Non-Parametric Morphology

To measure the half-light radii of the SMGs, we employ a curve of growth approach that invokes no assumptions about the underlying structure to the galaxy's light distribution. We adopt this approach because SMGs have long been assumed to originate from merger-driven events with clumpy unstable gas-rich disks, (e.g., Smail et al. 1998; Greve et al. 2005; Tacconi et al. 2008; Engel et al. 2010) and therefore the galaxy's morphology may deviate from simple parametric profiles.

We first perform a curve of growth analysis in each of the JWST bands from 0.9μm to 18μm. This is achieved by fitting a Gaussian profile to the cutout of each galaxy, allowing the centroid (x, y), axis ratio (b/a) and position angle (PA) to vary. We note the original centroid of the cutout is derived from the SEP source detection on the stacked F277W+F356W+F444W NIRCam bands (Section 3.2), and thus may not be the apparent centre of the galaxy at shorter wavelengths. A curve of growth is then derived in each band using ellipses which align to the galaxy's axis ratio and position angle. From the curve of growth, we measure the convolved radii containing 20, 50 and 80 per cent of the flux of each galaxy. The intrinsic radii of the galaxies are derived by de-convolving the sizes with the PSF in each band, measured through a similar curve of growth analysis.

To provide more quantitative, non-parametric, morphological indicators, we use the STATMORPH[4] code (Rodriguez-Gomez et al. 2019) which measures the Concentration, Asymmetry and Clumpiness (C, A, S; Abraham et al. 2003; Lotz et al. 2008) parameters that quantify how concentrated, asymmetrical and clumpy the galaxies' surface brightness profiles are, with higher values indicating more concentrated, asymmetric, or clumpier light profiles. We run STATMORPH on both SMG and field samples in all JWST bands using the same segmentation maps and PSFs as for the growth curve analysis described above.

In addition, the Gini and M_{20} parameters are also derived (for full definitions see Lotz et al. 2004; Snyder et al. 2015). Briefly,

the Gini parameter defines the pixel distribution of the galaxy's light, where $G = 1$ corresponds to all of the light concentrated in one pixel whilst $G = 0$ indicates each pixel contributes equally. The M_{20} parameter measures the second moment of the brightest 20 percent of pixels in the galaxy. This is normalised by the total moment for all pixels. Highly negative values indicate a high concentration of light, not necessarily at the centre of the galaxy. To validate the robustness of the STATMORPH measurements we compare the half-light radius to that derived from our growth curve analysis. We derive a median growth curve to STATMORPH median half-light radius ratio of $R_{\text{h,GC}} / R_{\text{h,statmorph}} = 1.06 \pm 0.01$ with a $16^{\text{th}}-84^{\text{th}}$ percentile range of $R_{\text{h,GC}} / R_{\text{h,statmorph}} = 0.93 - 1.45$ for the field sample in the F444W band. This indicates good agreement between the two independent morphological measurements[5].

3.6.3. Parametric Morphology

To quantify both the parametric morphological profiles of the galaxies and the deviations from these, we use the GALFITM code (Häußler et al. 2013). GALFITM is a Python-wrapper for GALFIT (Peng et al. 2010), that allows multi-component parametric models to be fit to a galaxy's multi-wavelength light distribution. For our analysis we use a single Sérsic model, convolved with the PSF of the relevant JWST band. We fit each band independently thus allowing us to constrain the intrinsic wavelength dependence of the galaxy's morphology.

To constrain the accuracy of the parametric analysis, we compare the GALFITM Sérsic index (n) to that derived by STATMORPH for the field galaxies in the NIRCam F444W band. We establish a median ratio of $n_{\text{F444W,GalfitM}} / n_{\text{F444W,statmorph}} = 1.00 \pm 0.01$ and a $16^{\text{th}}-84^{\text{th}}$ percentile range of $n_{\text{F444W,GalfitM}} / n_{\text{F444W,statmorph}} = 0.81 - 1.26$, indicating good agreement between the two independent codes.

Although a parametric Sérsic fit can model the overall distribution of a galaxy's light profile, it is the deviations from this simple profile (residuals) that encode important information about the detailed structure of the galaxies. To quantify the residuals we use the residual flux fraction (RFF), as defined in Hoyos et al. (2011, 2012),

$$\text{RFF} = \frac{\sum_{i,j \in A} |I_{i,j} - I_{i,j}^{\text{model}}| - 0.8 \times \sum_{i,j \in A} \sigma_{\text{Bkg}\,i,j}}{\sum_{i,j \in A} I_{i,j}} \quad (1)$$

where the sum is performed over all pixels within 2.5 times the Kron radius, as derived in Section 3.2. $|I_{i,j} - I_{i,j}^{\text{model}}|$ is the absolute value of pixel i, j's residuals to model Sérsic model fit, whilst $\sum_{i,j \in A} I_{i,j}$ indicates the total flux measured in the source as defined in Section 3.2. The 0.8 factor multiplied by the sum over the background rms of the region $(\sigma_{Bkg\,i,j})$, ensures that a blank image with constant variance has a RFF = 0.0 (see Hoyos et al. (2012) for details).

It is well known that morphological codes such as GALFITM and STATMORPH systemically underestimate the uncertainties on the derived morphological parameters (e.g., van der Wel et al. 2012, 2024). To overcome this we employ an empirical approach which utilises the unique wavelength coverage of the NIRCam observations in the PRIMER Survey. Specifically, the majority of field galaxies (816/850) and SMGs (75/80) in our sample have both F410M and F444W observations. The F410M is a medium

---

[4] https://statmorph.readthedocs.io/en/latest/

[5] We note however we expect some variation between the two methods due to the definitions of centroid and total fluxes used (see Lotz et al. 2004)
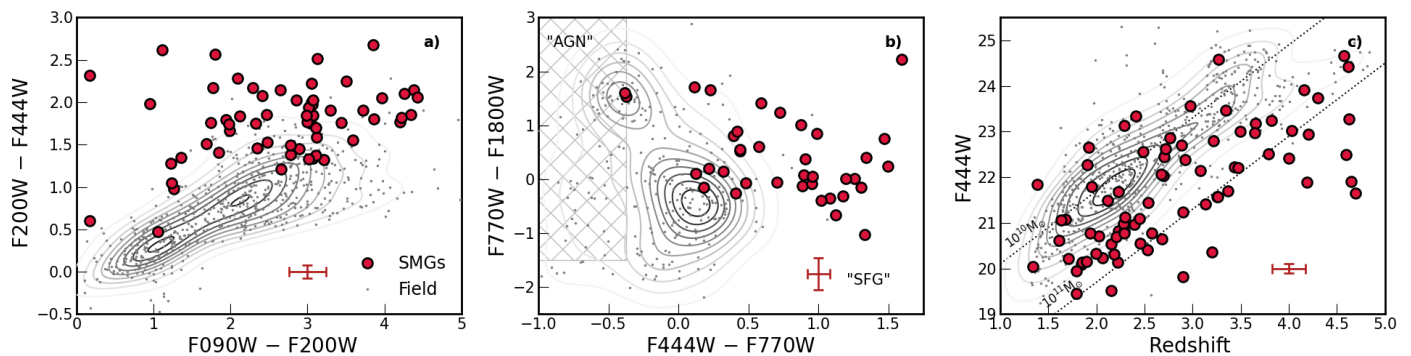
Fig. 4: The distribution of NIRCam colours (F200W−F444W versus F090W−F200W) *(a)*, MIRI colours (F770W−F1800W versus F444W−F770WW) *(b)* and F444W AB magnitude as a function of redshift *(c)*, with lines of constant stellar mass overlaid. A representative error bar is indicated in the lower-right corner of each panel. Panel *a)* demonstrates the SMGs are much redder than the field population, as expected. Panel *b)* highlights that a fraction of SMGs and field galaxies may in fact host AGN with a very red F770W−F1800W colour and bluer F444W−F770W indicating a strong upturn in the SED beyond rest-frame 3μm. We label the "AGN" and star-forming galaxy ("SFG") regions in the colour space adapted from Kirkpatrick et al. (2013, 2017). We note the F770W−F1800W > 1 colour can also be driven by the 6.2μm PAH feature detected in the F18000W filter at $z \sim 1.9$. Panel *c)* demonstrates that the SMGs are the most massive (brightest) galaxies at their epoch with field selected to be the most massive low far-infrared luminosity galaxies.

band filter covering the observed-frame 3.8 – 4.3μm emission, whilst the wide-band F444W filter is sensitive to the 3.8 – 4.9μm emission. Thus, for each galaxy with observations in both filters, we can make two independent measures of the galaxy's morphology at very similar rest-frame wavelengths. Analysing the variance in morphological parameters between the two filters as a function of signal-to-noise allows us to infer a representative uncertainty on the morphological parameters at a given wavelength for each source given its signal-to-noise in that band. We use this conservative approach to quantify the uncertainties in the following analysis.

4. Results and Discussion

From an initial sample of 88 SMGs, we have constructed a sample of 80 non-lensed SMGs with reliable (S/N > 4.5) ALMA 870μm detections and multi-wavelength HST and JWST coverage from 0.4 – 18 μm. Full details of the wavelength coverage for the individual SMGs in our sample are given in Appendix A. From the initial sample, we omitted two strongly lensed SMGs due to uncertainties on the photometry and structural properties introduced by the lensing configuration of each source. Identifying $2 \pm 2\%$ of SMGs in our sample are affected by foreground galaxy lensing matches the prediction of Chapman et al. (2002), that between 3 and 5 per cent of submm sources identified in blank-field SCUBA observations would be affected by lensing.

For the 60 SMGs with HST coverage, we detect no F160W counterpart at S/N < 3 in 10 sources. All of them have clear near-infrared counterparts in the NIRCam F444W band at S/N > 5, whilst three also have a S/N > 3 in the NIRCam F150W band. This leaves seven "NIR-faint" (sometimes imprecisely described as "HST-dark") SMGs with no detection in the *H*-band (S/N < 3). These seven SMGs have significant levels of dust attenuation as derived from MAGPHYS with $A_V > 3.9$. This indicates that whilst the significant dust content of these galaxies can lead to their dark nature in HST observations, it is also driven by the lack of sensitivity and depth of previous observations.

Of the 78 SMGs with NIRCam-SW coverage, we identify one galaxy, AS2UDS0346.0 at $z = 4.1$, that is undetected (S/N < 3) blueward of 2.7μm and is first detected by JWST in the

F277W band at S/N ≥ 5. From our MAGPHYS analysis we derive significant dust attenuation with $A_V = 5.1$ for AS2UDS0346.0 with a stellar mass of $\log_{10}(M_*[M_\odot]) = 11.2$ that is representative of our sample. For SMGs with suitable NIRCam coverage we identify detections (S/N > 3) in F090W for 59% (43/73), in F150W for 87% (68/78) and in F200W for 96% (70/73) of the sources respectively. All have S/N > 3 detections in the NIRCam-LW and MIRI bands.

In Figure 4 we investigate the photometric properties of the SMGs in the JWST bands by comparing the NIRCam and MIRI colours. Specifically, in Figure 4a we compare the NIRCam F200W−F444W colour with the F090W−F200W colour. At the median redshift of the SMG and field galaxies, these filters sample the rest-frame *UVJ* regime of the galaxies' spectral energy distributions, highlighting the distinct red nature of the SMGs compared to the general field. Given this nature, it may be possible by colour selection to identify the JWST counterpart to the sub-millimetre bright SCUBA-2 source without requiring higher resolution ALMA observations (e.g., Alberts et al. 2013; Chen et al. 2016; An et al. 2018; Hwang et al. 2021). To investigate this, for each SMG we compare the NIRCam F200W − F444W colour of all sources detected in the 14.8 arcsecond SCUBA-2 beam to that of the ALMA-selected SMG. In 51% (41/80) of the SCUBA-2 observations, the ALMA source represents the reddest source in the beam. This indicates that whilst colour is a good identifier of SMGs, further information such as proximity to beam centre, predicted 870μm fluxes and multi-wavelength observations from infrared to radio are required to isolate the exact near-infrared counterpart (e.g., Downes et al. 1986; Ivison et al. 2002; Hodge et al. 2013; Casey et al. 2013; Gillman et al. 2023).

Figure 4b compares the MIRI and NIRCam colours with the F770W−F1800W colour shown as a function of F444W−F770W colour. At the median redshift of the SMG and field galaxies, these filters sample the rest-frame near and mid-infrared. The SMGs on average have redder F444W−F770W colours with comparable F770W−F1800W colours to the field population, reflecting the dust attenuation of the shorter wavelength light. The SMGs and field galaxies which exhibit very red F770W−F1800W colours with bluer F444W−F770W colour
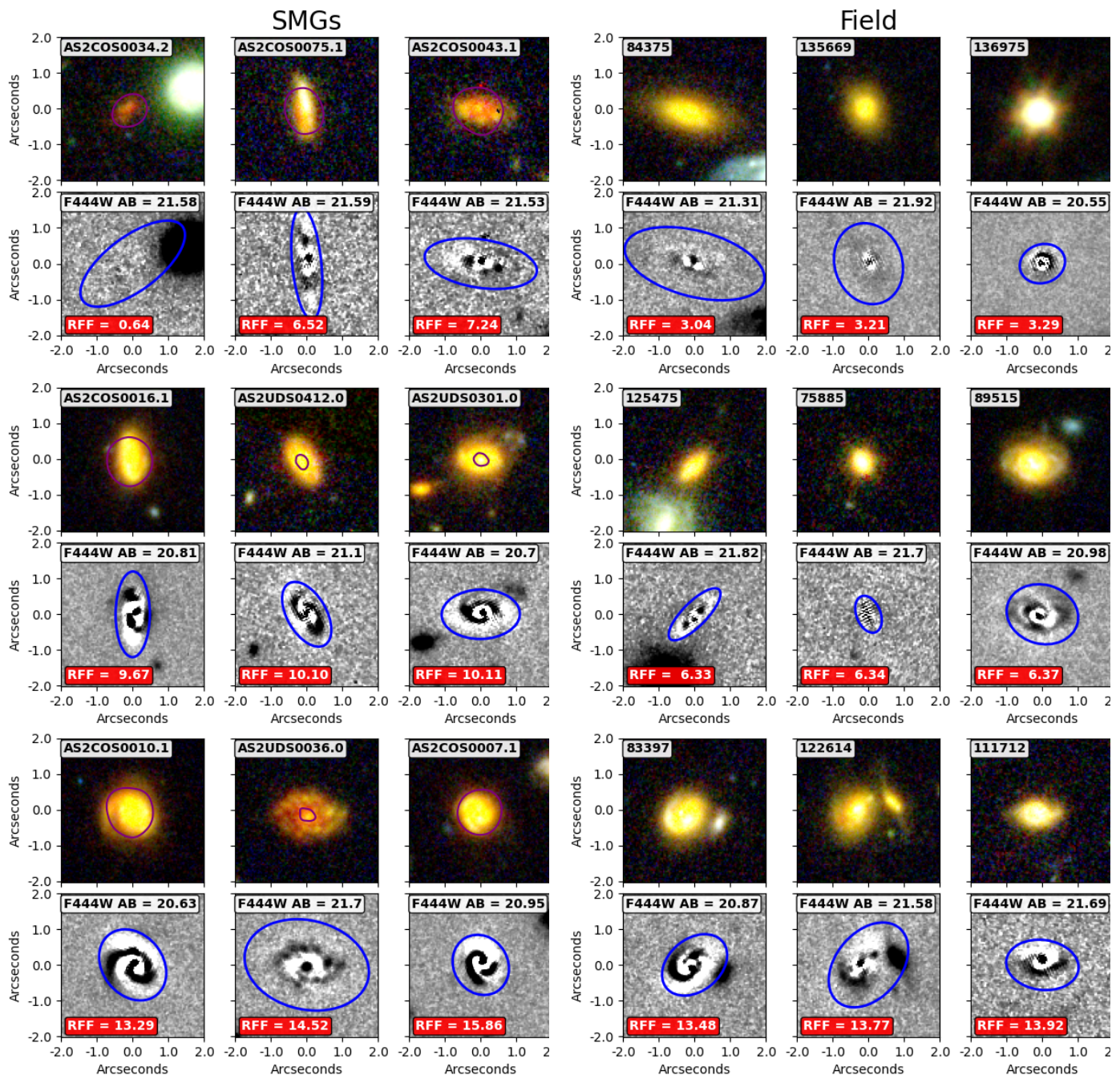
Fig. 5: For both SMGs (*left*) and field galaxies (*right*) we show the examples of the F356W/F277W/F115W RGB-colour image. For the SMGs we overlay the ALMA 870μm 11σ contour (*purple*) from Stach et al. (2019) or Simpson et al. (2020). In the lower panel of each source, we show the residuals of the GALFITM single Sérsic model fit. The blue ellipse marks the region within which we calculate the residual flux fraction (RFF) of the Sérsic fit, as quantified in the lower-left corner of each panel. The galaxies are selected to have an F444W AB magnitude of $m_{F444W} = 20 - 22$ and are ranked from low-to-high RFF. No clear distinction is identified in the F444W RFF values between the SMGs and field galaxies.

may indicate the presence of Active Galactic Nuclei (AGN) as noted by Ivison et al. (2004) who used MIPS/24μm and IRAC colours to identify AGN and starburst galaxies. We highlight the regions of the colour diagram that an "AGN" or star-forming galaxy ("SFG") would likely inhabit, adapted from Kirkpatrick et al. (2013, 2017). Of those with MIRI coverage, we identify $24 \pm 5\%$ (69/282) of the field galaxies have near-infrared colours that may indicate the presence

of AGN activity whilst for the SMGs we establish a lower fraction of $3 \pm 1\%$ (2/37). The two SMGs with "AGN" like colours, AS2UDS0259.0 and AS2UDS0659.0, both exhibit extended morphologies in the MIRI F770W and F1800W observations with no visible point source, indicating any contribution from an AGN is minimal. This is in agreement with previous studies which identify the AGN contribution in SMGs to be small (e.g., Stach et al. 2019). The one SMG with a com-

pact, point-source like morphology, AS2UDS0173.0, is not covered by the MIRI observations. The SFG and AGN classification in Figure 4b does not fully encapsulate the bi-modality present in the colour space, especially in the field galaxies. Galaxies with F1800W−F770W>1 and F444W−F770W<0, represent a bright ($m_{F444W} = 21.5 \pm 0.1$) lower redshift subset ($z = 1.9 \pm 0.04$) with significantly brighter F1800W emission ($m_{F1800W} = 20.3 \pm 0.1$) compared to the "bluer" population ($z = 2.9 \pm 0.1$, $m_{F444W} = 22.9 \pm 0.1$, $m_{F1800W} = 23.3 \pm 0.1$). At $z = 1.9$, the F1800W filter is sensitive to the 6.2μm PAH feature, which can strongly enhance the mid-infrared emission in massive galaxies, resulting in red F770W−F1800W colours (e.g., Draine et al. 2007; Aniano et al. 2020; Shivaei et al. 2024).

In Figure 4c we show the correlation between NIRCam F444W magnitude and the redshift of the galaxies. We overlay lines of constant stellar mass, highlighting that the SMGs are the most massive galaxies at their epoch (Dudzevičiūtė et al. 2020) with the field selected to massive with lower far-infrared luminosity.

4.1. Near-Infrared Morphology

While SMGs have long been known to exhibit complex, potentially merger-like, morphologies based on rest frame *UV* imaging (e.g., Smail et al. 1998; Chapman et al. 2004; Swinbank et al. 2010; Aguirre et al. 2013) the influence of dust has meant the true stellar morphologies are still unknown. The combination of near-infrared colour images (Figure 1) and F444W Sérsic fit residual maps (Figure 5) provides an unprecedented insight into the embedded stellar structures and asymmetries in the SMGs.

For 21/80 SMGs, from a visual inspection, we identify clear spiral or tidal arm features in the Sérsic model residuals, as well as clear clumpy structures in $30 \pm 4\%$ (24/80) of the SMGs. In particular, one galaxy AS2UDS0259.0, shows a clear bar-like structure in the F444W image indicating complex multi-phase structures may be present, similar to those identified in recent JWST and ALMA studies (e.g., Hodge et al. 2019; Smail et al. 2023; Rujopakarn et al. 2023; Liu et al. 2023).

We estimate that $40 \pm 10\%$ (32/80) of the SMGs are isolated systems, with no strong perturbations or obvious neighbours on $\simeq 20 - 30$ kpc (projected) scales, while 16 SMGs ($20 \pm 5\%$) in our sample have potential companions or are interacting with another massive galaxy suggesting major mergers, the remaining 32 SMGs ($40 \pm 10\%$) have faint companions and show signs of disturbance (e.g., asymmetries in the GALFIT F444W residuals) that suggest potential minor interactions and mergers. The median far-infrared luminosity of the candidate major mergers is $L_{IR} = 10^{12.53\pm0.05} L_{\odot}$, compared to $L_{IR} = 10^{12.49\pm0.05} L_{\odot}$ for the remainder of the sample, indicating no strong dependence of far-infrared luminosity on merger state (e.g., Hopkins et al. 2010). Indeed, an equivalent visual classification of the less active field sample returns very similar merger statistics with $25 \pm 5\%$ of the sample showing evidence for potential major mergers and the remaining $\sim 75\%$ showing much weaker or no evidence for merger-related disturbance or companions on $\simeq 20$–30 kpc scales. This similarity in the rate of mergers between SMGs and less active galaxies is consistent with the theoretical results from the EAGLE simulation from McAlpine et al. (2019) who found that simulated SMGs had similar rates of recent mergers to less active galaxies, in part because most galaxies at high redshifts are undergoing continuous infall and merging.

To summarise, while signs of potential dynamical disturbance are frequently seen in our SMG sample, we conclude that the majority of SMGs do not appear to be the result of

late-stage, major mergers. This is in contrast with the situation for similar far-infrared luminous populations at $z \sim 0$, where systems with far-infrared luminosities of $L_{IR} \geq 10^{12} L_{\odot}$ are frequently associated with late-stage major mergers (e.g., Sanders et al. 1988; Farrah et al. 2001), although there are claims that this fraction declines at $z \sim 1$ (e.g., Kartaltepe et al. 2010), with an increasing fraction of starburst galaxies appearing to be isolated systems (e.g., Faisst et al. 2024). It is also in contrast to early studies of SMGs with resolved CO kinematics (e.g., Engel et al. 2010) as well near-infrared spectroscopic observations (e.g., Alaghband-Zadeh et al. 2012; Drew et al. 2020) which suggested that the majority of SMGs are mergers, with distinct separated dust-detected components. There are at least two such examples in our sample of SCUBA-2 sources, AS2UDS0322 and AS2COS0034, and one ALMA source (AS2UDS0071.0) that comprise multiple ALMA-detected, or NIRCam-F444W detected, galaxies that show clear signs of galaxy interactions with AS2COS0034 comprising two SMGs that are both detected in [CII] emission at $z_{[CII]} = 4.62$ (Mitsuhashi et al. 2021).

4.1.1. Sizes, Sérsic Indices and Axis Ratios

We measure the half-light radius of the SMGs and field galaxies in the F444W band, determining median values of $R_h = 2.70 \pm 0.23$ kpc and $R_h = 2.50 \pm 0.10$ with $16^{th} - 84^{th}$ percentile ranges of $R_h = 1.82 - 4.36$ kpc and $R_h = 1.64 - 3.76$ kpc respectively. To establish whether the SMGs and field galaxies are drawn from the same underlying distribution, we perform a Kolmogorov-Smirnov (KS) test on the mass normalised distributions of half-light radius. To mass normalise the half-light radius distributions, we adopt the rest-frame optical mass size relation from Ward et al. (2024) at $2 < z < 3$. From the median stellar mass of the field galaxies to the median stellar mass of the SMG sample, we derive an increase in half-light radius of $27 \pm 6\%$, which we apply to the field galaxies' half-light radii to account for the offset in stellar mass between the two samples. For the non-Gaussian distributions of SMG and field galaxy morphological properties, we require $p_{KS} \leq 0.003$ ($>3\sigma$) to confirm the populations are inherently different. We conclude the SMGs and field galaxies have indistinguishable distributions of mass normalised half-light radius with $p_{KS} = 0.06$.

In Figure 6 we show the correlation between stellar mass and F444W half-light radius for both field and SMGs. We overlay the rest-frame optical mass size relation for star-forming galaxies at $2 < z < 3$ from Ward et al. (2024). On average, the field galaxies follow the trend identified by Ward et al. (2024), whilst the SMGs, as indicated by the running median in Figure 6, exhibit marginally smaller F444W sizes for stellar masses above $\log_{10}(M_*[M_{\odot}]) > 10.5$. We note however, the majority of galaxies used to define the mass size relation in Ward et al. (2024) have a stellar mass of $\log_{10}(M_*[M_{\odot}]) < 10.5$. In panel *b)* of Figure 6, we compare the distribution Sérsic index for the field sample to those of the SMGs, identifying more disc-like Sérsic indices for the SMGs with a median of $n_{F444W} = 1.10 \pm 0.10$ and a $16^{th} - 84^{th}$ percentile range of $n_{F444W} = 0.63 - 1.98$ whilst the field galaxies have a higher median value of $n_{F444W} = 1.85 \pm 0.07$ with a $16^{th} - 84^{th}$ percentile range of $n_{F444W} = 0.88 - 4.35$. Applying a KS test, we identify the two distributions are distinctly different with a $p_{KS} < 0.001$.

From our non-parametric analysis, we derive a median axis ratio of $b/a = 0.55 \pm 0.03$ for the SMGs and a $16^{th} - 84^{th}$ percentile range of $b/a = 0.37 - 0.82$ in the NIRCam F444W band. This is comparable to the axis ratio distribution for 870μm dust continuum in SMGs with $b/a = 0.63 \pm 0.02$ (Gullberg et al.
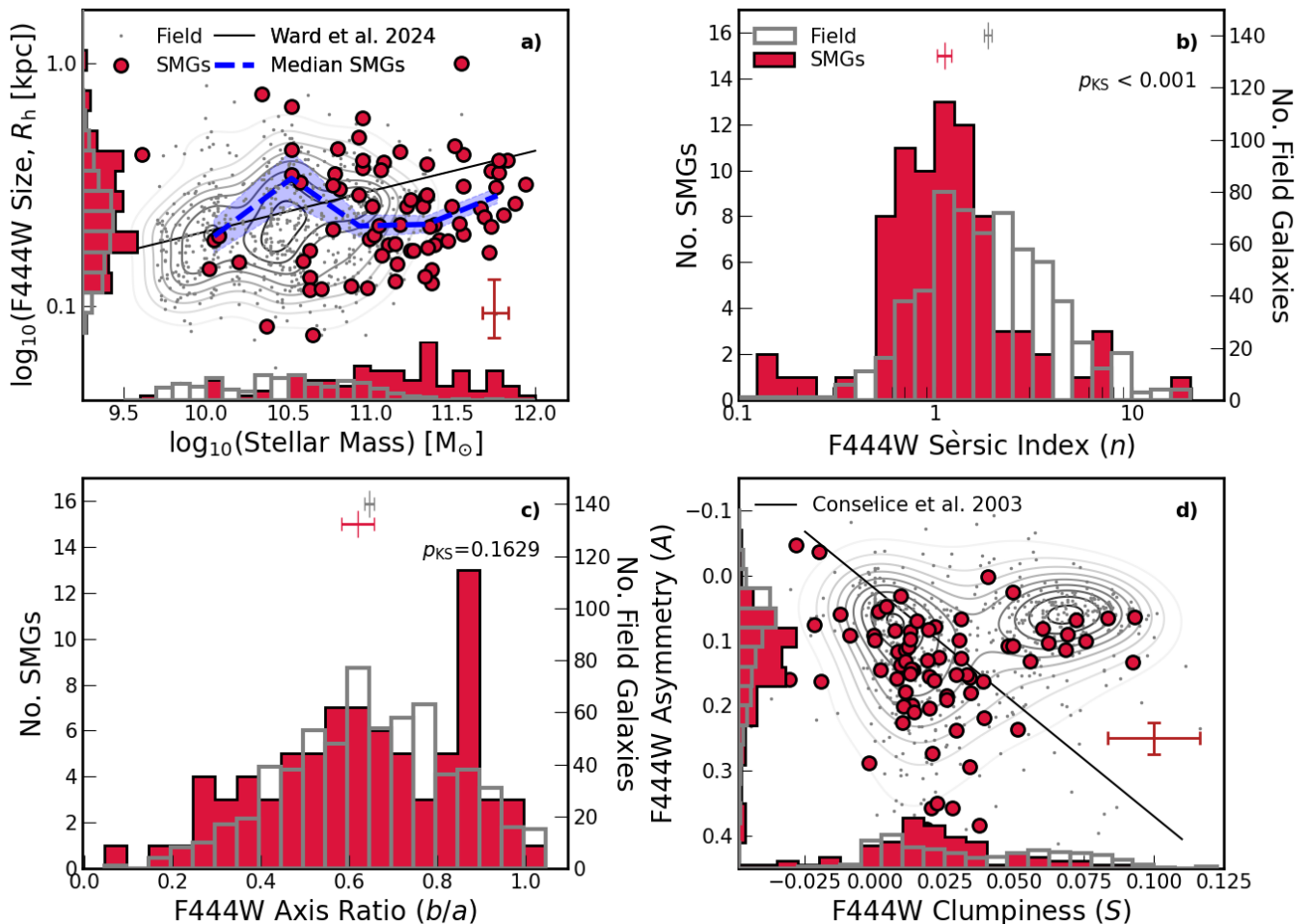
Fig. 6: The correlation between *a)* stellar mass and half-light radius, and *d)* the Clumpiness (S) and Asymmetry (A) for the SMG and field sample in the NIRCam F444W filter. In each panel we show histograms of each parameter for the field (*open grey*) and SMG sample (*red histograms*). In panel *a)* we also overlay the mass size relation for $2 < z < 3$ star-forming galaxies from Ward et al. (2024) and in panel *d)* the relation between Asymmetry and Clumpiness identified by Conselice et al. (2003). In panels *b)* and *c)* we show the distributions of Sérsic index (n) and axis ratio (b/a) in the F444W band. For each distribution, we display the KS probability (p_{KS}) that the two distributions are drawn from the same parent population, where $p_{KS} < 0.001$ suggests a significant difference in the distributions. We plot the bootstrap median and uncertainty for the two distributions at the top of each panel. The SMGs, on average, have comparable sizes ($p_{KS} = 0.06$) and lower Sérsic indexes ($p_{KS} < 0.001$) than less active field galaxies, whilst exhibiting similar axis ratios ($p_{KS} = 0.16$) and clumpiness ($p_{KS} = 0.02$) with higher asymmetry ($p_{KS} < 0.001$).

2019). For the field galaxies, we derive a median F444W axis ratio of $b/a = 0.53 \pm 0.01$ and $16^{th} - 84^{th}$ percentile range $b/a = 0.31 - 0.77$. The distribution of axis ratios, as shown in Figure 6, is comparable to that of the SMGs with $p_{KS} = 0.16$. The SMGs distribution reflects more that of the disk+spheroid classification found in recent optical studies of high-redshift galaxies (e.g., Kartaltepe et al. 2023; Pandya et al. 2024) with a median value of $b/a = 0.51$ and $16^{th} - 84^{th}$ percentile range of $b/a = 0.35 - 0.68$.

4.1.2. Residuals, Clumpiness and Asymmetry

Whilst the Sérsic profiles indicate more disc-like surface brightness distributions for the SMGs, it is the deviations from the parametric light profiles, as quantified by the RFF parameter, that encodes the unique morphological properties of each galaxy. In Figure 5, we show examples of the NIRCam F444W Sérsic model residuals, and the derived RFF values,

for both SMGs and field galaxies. Whilst some galaxies exhibit smooth residuals, and low RFF values, several galaxies (both SMGs and field) display complex morphologies with multiple clumps, spiral arms or bright compact point sources. For the SMGs we identify a median RFF value in the F444W band of $RFF^{F444W} = 10.2 \pm 0.5$ with a $16^{th} - 84^{th}$ percentile range of $RFF^{F444W} = 5.9 - 16.3$ whilst the field galaxies have a median value of $RFF^{F444W} = 8.5 \pm 0.2$ with a $16^{th} - 84^{th}$ percentile range of $RFF^{F444W} = 4.5 - 17.2$. We compare the distributions of RFF for SMGs and field galaxies finding a KS-statistic of $p_{KS} = 0.002$, indicating the are distinguishable at $>3\sigma$ level.

Although the 870μm ALMA observations of the majority of the SMGs in our sample are not high enough resolution (FWHM $\leq 0\rlap{.}''2$) to identify these structural features, high-resolution sub-millimetre studies have identified spiral arms, bars and star-forming rings embedded in exponential dust disks (e.g. Hodge et al. 2019; Amvrosiadis et al. 2024). For a subset of the SMGs (15/80), however, $0\rlap{.}''2$ resolution ALMA 870μm
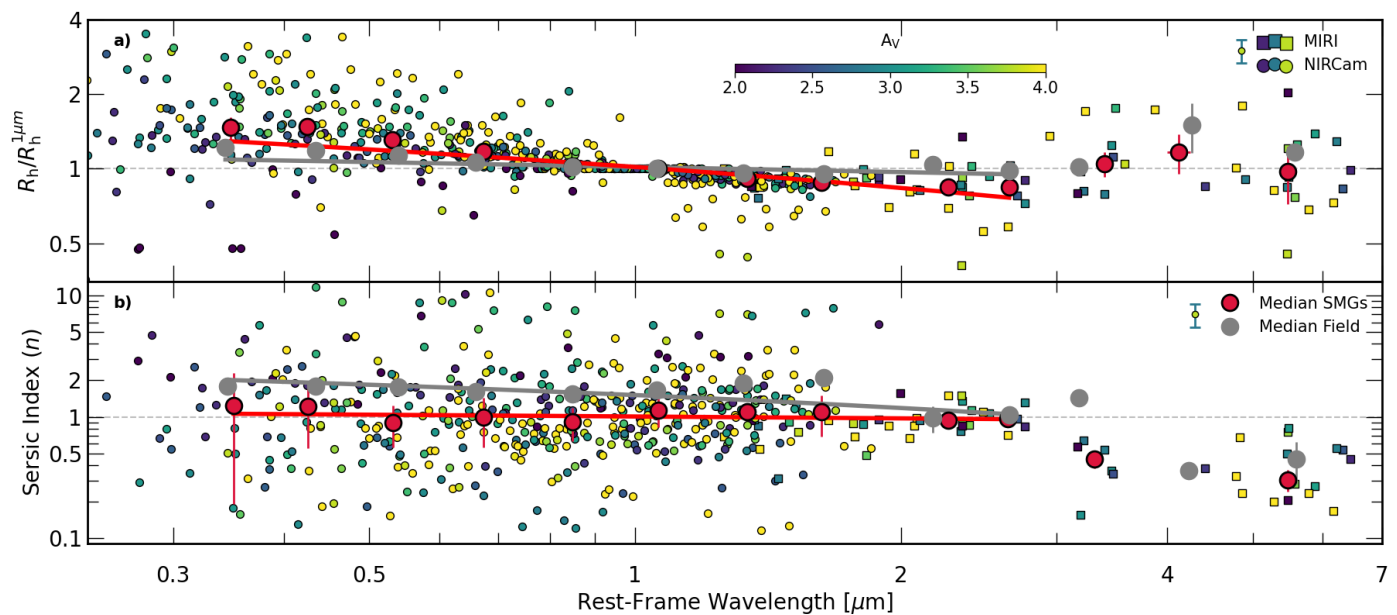
Fig. 7: *Top:* The growth curve half-light radius (R_h) of the SMGs, normalised by the rest-frame 1μm half-light radius of the respective galaxy as a function of rest-frame wavelength and colour-coded by the galaxy integrated A_V. We show individual measurements for SMGs, and a representative error bar, as well as the running median for the field sample. *Bottom:* Sérsic index derived from the GALFITM parametric fitting as a function of rest-frame wavelength. We indicate the NIRCam measurements by circles and MIRI measurements by squares. We show a running median, and standard error ($\sigma/\sqrt{n}$) in fixed logarithmic bins of wavelength for the SMGs and field galaxies. In both panels, we plot the parametric fit for the field (solid grey line) and SMGs (solid red line). We find that the SMGs, on average, have a stronger size variation with wavelength, becoming more compact at longer wavelengths quicker than field galaxies, whilst exhibiting lower Sérsic index at all wavelengths.

observations are available as presented in Gullberg et al. (2019). These resolved observations are insufficient to identify complex dust structures, but the resolved 870μm emission's morphology provides insight into any underlying structural features. For these 15 SMGs we first compare the ALMA 870μm size measured in the *uv*-plane to the F444W growth curve size. We estimate a median ratio of $R_\mathrm{h}^{\mathrm{F444W}} / R_\mathrm{h}^{870\mu m} = 2.7 \pm 0.4$ with a $16^{\mathrm{th}} - 84^{\mathrm{th}}$ range of $R_\mathrm{h}^{\mathrm{F444W}} / R_\mathrm{h}^{870\mu m} = 1.5 - 3.5$. As identified by previous studies the far-infrared emission is much more compact than the emission at bluer wavelengths (e.g. Simpson et al. 2015; Lang et al. 2019; Gullberg et al. 2019). We perform a Spearman rank test on the correlation between F444W/870μm size ratio and the A_V of the galaxy, identifying no significant correlation ($p_{\mathrm{SR}} = 0.33$). However, a larger sample is required to robustly conclude the lack of correlation.

To investigate the presence of complex dust structures we compare the 870μm axis ratio and position angle to that derived for the F444W emission. For the 870μm emission we adopt the free Sérsic fitting parameters from Gullberg et al. (2019). We identify median ratios of $b/a_{\mathrm{F444W}} / b/a_{870\mu m} = 0.95 \pm 0.11$ and $PA_{\mathrm{F444W}} / PA_{870\mu m} = 0.94 \pm 0.12$, indicating good agreement in the alignment of the near-infrared (rest-frame $\approx$ 1μm) and far-infrared (rest-frame $\approx$ 250μm) emission, suggesting they are tracing the same underlying structure, in contrast to the UV/optical and far-infrared offsets identified in previous multi-wavelength high-resolution studies (e.g., Chen et al. 2015; Calistro Rivera et al. 2018; Hodge et al. 2019).

In panel *d)* of Figure 6, we show the correlation between asymmetry (A) and clumpiness (S) in the NIRCam F444W band as derived from STATMORPH and over plot the relation between

A and S derived by Conselice et al. (2003)[6]. We identify the SMGs and field galaxies have similar clumpiness with a median value of $S_{\mathrm{F444W,SMGs}} = 0.02^{+0.03}_{-0.02}$ and $S_{\mathrm{F444W,field}} = 0.03^{+0.04}_{-0.04}$ respectively with a $p_{\mathrm{KS}} = 0.02$, indicating they are broadly consistent with being drawn from similar distributions. The asymmetry in the F444W band for the SMGs is higher with a median value of $A_{\mathrm{F444W,SMGs}} = 0.13^{+0.09}_{-0.06}$ compared to the field galaxies ($A_{\mathrm{F444W,field}} = 0.08^{+0.12}_{-0.06}$) and a $p_{\mathrm{KS}} < 0.001$, indicating the two distributions are distinct.

The correlation between asymmetry and clumpiness highlights two clear regions. At constant asymmetry, there are two populations, one at low clumpiness ($S < 0.04$) and one at high clumpiness ($S > 0.04$), where the majority of the SMGs and field galaxies have low clumpiness with smooth, symmetric light distributions whilst those galaxies at high clumpiness show signs of concentrated star-forming regions. The SMGs at $S > 0.04$ are more compact in the F444W filter with a median size of $R_\mathrm{h} = 1.72 \pm 0.14$ kpc compared to the SMGs with lower clumpiness ($S < 0.04$) with a median size of $R_\mathrm{h} = 2.96 \pm 0.25$ kpc, whilst exhibiting comparable other morphological and MAGPHYS derived properties. We note that several studies have highlighted the uncertainty introduced in non-parametric morphological measurements when the Petrosian radius of the galaxy (R_p) is comparable to the FWHM of the observations (e.g., Yu et al. 2023; Ren et al. 2024), especially when the clumpiness parameter is measured between $0.25R_\mathrm{p}$ and $1.5R_\mathrm{p}$, see Lotz et al. (2004) for details.
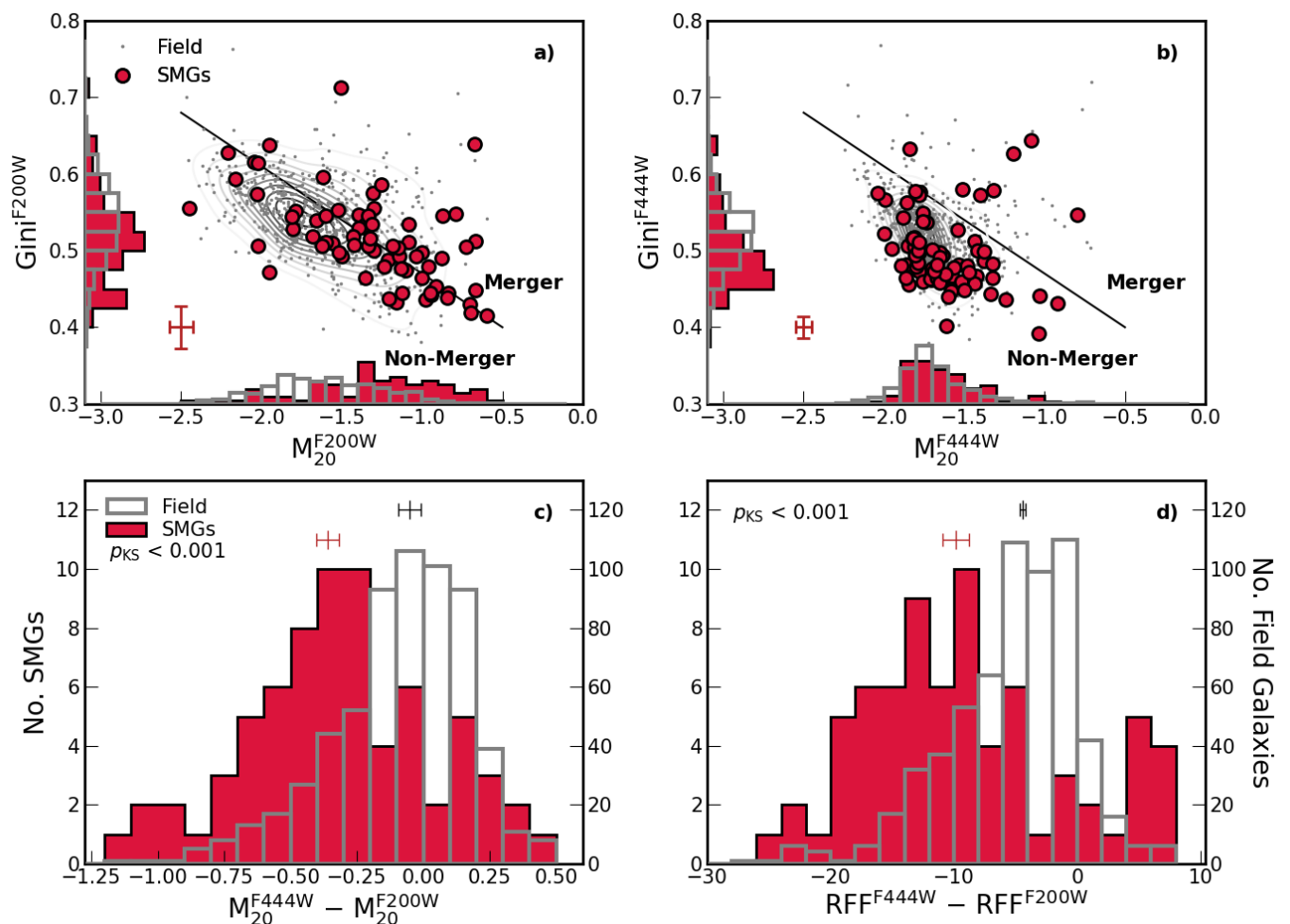
Fig. 8: We show the Gini – M_{20} relation for the field galaxies (grey dots and contours) and SMG sample (red circles), in the *a)* F200W and *b)* F444W bands as well as histograms showing the distribution of each parameter on each axis. The solid-black line indicates the boundary line between mergers and non-mergers as defined in Lotz et al. (2008). Both SMGs and field galaxies scatter about the line in the F200W band whilst the majority lie in the non-merger region of the equivalent F444W plot. In panels *c)* and *d)* we show the distributions of $M_{20}^{F444W} - M_{20}^{F200W}$ and $RFF^{F444W} - RFF^{F200W}$. For each distribution, we indicate the KS-statistic showing that the SMGs have a stronger variation in morphology with wavelength with higher RFF and M_{20} values at 2μm than 4μm indicating more structure in the residuals and disturbed morphologies.

4.2. Wavelength Dependent Morphology

The preceding analysis of the SMGs and field galaxies stellar (near-infrared) morphologies has revealed broad similarities between the two populations. Many previous studies suggest the extreme properties of SMGs originate from merger-driven events (e.g., Smail et al. 1998; Swinbank et al. 2010; Aguirre et al. 2013). We do not expect the morphological signatures of these mergers to show wavelength dependence in contrast to the effects of dust. Thus, by quantifying the morphological variation with wavelength in the field and SMG sample, we can test the legitimacy of the merger-driven scenario.

For the SMGs and field galaxies we measure a median F200W half-light radii of $R_{h,F200W} = 4.0 \pm 0.3$ kpc and $R_{h,F200W} = 2.8 \pm 0.1$ kpc respectively. Compared to the F444W, for the SMGs this represents a 48% reduction in size between 2μm and 4μm whilst for the field galaxies the reduction in size is only 11%, although we note this comparison is not done at

_____

[6] The relation is corrected for the different definitions of clumpiness given by Lotz et al. (2004) and Conselice et al. (2003)

fixed stellar mass it highlights the variation of morphology with wavelength for the two samples. To further investigate the variation in the SMGs and field galaxy morphology as a function of wavelength, in Figure 7 we correlate the half-light radius, normalised by the rest-frame 1μm half-light radius, and Sérsic index with the rest-frame wavelength probed by the NIRCam and MIRI observations.

Below 1μm, for SMGs in Figure 7 there is increased spread in half-light radius with an apparent correlation with dust content quantified by A_V. At rest-frame wavelengths greater than 3μm where we use the MIRI F770W and F1800W bands to quantify the morphology, we identify a decrease in the median Sérsic index of both field and SMGs to $n \sim 0.4$ and an increase in the half-light radius. We suspect this trend is driven by the larger beam size of the MIRI observations with FWHM = 0″.27 and 0″.59 respectively for the F770W and F1800W filters, in addition to the shallower depth compared to the NIRCam observations, resulting in a more smoothed, less-structured, light distribution. In addition, in the rest-frame near-infrared (> 3μm) any AGN compo-

nent that is present in the galaxy starts to be more prominent over the stellar emission, with point-source ($n \sim 0.5$) morphology.

To quantify the field galaxy and SMGs size evolution with wavelength, we perform fits to the median values shown in Figure 7 up to rest-frame 3μm using an orthogonal distance relation (ODR) algorithm that takes into account the uncertainties on the median values in both wavelength and size. We define the function as,

$$\frac{R(\lambda)}{R_{1\mu m}} = R_0 + \frac{d(R_h/R_{1\mu m})}{d\lambda} \log_{10}(\lambda), \quad (2)$$

where λ is the rest-frame wavelength probed by the observations. For the SMGs we derive a slope of $\frac{d(R_h/R_{1\mu m})}{d\lambda} = -0.60 \pm 0.09$ and $R_0 = 1.02 \pm 0.02$, whilst for the field galaxies we estimate $\frac{d(R_h/R_{1\mu m})}{d\lambda} = -0.15 \pm 0.07$ and $R_0 = 1.02 \pm 0.01$. This indicates the SMGs have stronger variation in size with wavelength, becoming more compact faster than typical field galaxies, as highlighted by the best-fit solution plotted in Figure 7. However, this trend may be driven by centrally concentrated dust inflating the rest-frame optical sizes of the SMGs resulting in a stronger observed variation with wavelength. To ensure size (R_h) variation with wavelength identified in the SMGs and field galaxies in Figure 7 is not driven by the redshift evolution of the galaxies, in Appendix C, we correlate the rest-frame 1μm size of the galaxies with their redshift. On average we identify a consistent redshift evolution in the near-infrared sizes of the SMGs and field galaxies, indicating redshift is not driving the morphological wavelength variation.

Furthermore Figure 7 shows the SMGs, on average, have a lower Sérsic index than the field galaxies at all wavelengths. To quantify the evolution of Sérsic index with wavelength we fit a similar relation to that used to quantify the size evolution of the form,

$$n(\lambda) = n_0 + \frac{dn}{d\lambda} \log_{10}(\lambda), \quad (3)$$

up to a rest-frame wavelength of 3μm. The median Sérsic index of the SMGs have an $\frac{dn}{d\lambda} = -0.12 \pm 0.11$ and $n_0 = 1.0 \pm 0.04$, whilst the field galaxies exhibit strong variation with wavelength, but at higher average Sérsic index ($\frac{dn}{d\lambda} = -1.10 \pm 0.23$ and $n_0 = 1.51 \pm 0.10$). Thus indicating on average, the SMGs have less centrally peaked light distributions, which may further be an indication of the central dust obscuration.

To further investigate the variation of morphology with wavelength in the SMG and field samples, in Figures 8a & b, we show the Gini $-$ M_{20} relation which has been used as a crude late-stage merger indicator (Lotz et al. 2008; Liang et al. 2024; Polletta et al. 2024) in the F200W and F444W bands. We select the F444W band as this most closely traces the stellar morphology of the galaxies, whilst F200W band corresponds to the rest-frame V-band for the median redshift of the samples, at a similar wavelength to the R-band where the Gini $-$ M_{20} "merger" and "non-merger" boundary was calibrated by Lotz et al. (2008). At 2μm (rest-frame V-band) both field and SMG samples scatter about the boundary between "merger" and "non-merger", with $40 \pm 5\%$ of the SMGs lying in the merger region. The SMGs are offset relative to the field though with higher M_{20} and lower Gini values. At 4μm (rest-frame z-band) almost all SMGs ($92 \pm 2\%$) and field galaxies lie in the "non-merger" region of the relation, with consistent Gini and M_{20} values. Between 2μm and 4μm the relative shift in the Gini $-$ M_{20} parameter space is larger for the SMGs than the field galaxies.

To understand the origin of this shift in the Gini-M_{20} plane, in Figure 8c we show the difference between the M_{20} parameter in the F444W and F200W bands. This plot highlights that

the SMGs have higher M_{20} in the F200W than F444W band which indicates SMGs have less concentrated F200W morphologies whilst the field galaxies have more similar M_{20} values between the two bands. The significance of the difference between the field and SMGs is further indicated by the KS-statistic value of $p_{ks} < 0.001$. To further highlight the reduction in structured emission between the F200W and F444W bands, in Figure 8d we show the difference between RFF in the two bands for the SMGs and field galaxies. On average the SMGs exhibit a greater difference in RFF across bands, with more significant F200W residuals, with a median value of $RFF^{F444W} - RFF^{F200W} = -10.0 \pm 1.0$ with a $16^{th} - 84^{th}$ percentile range of $RFF^{F444W} - RFF^{F200W} = 2.0 - 17.4$ whilst for the field galaxies the median is $RFF^{F444W} - RFF^{F200W} = -4.6 \pm 0.3$ with a $16^{th} - 84^{th}$ percentile range of $RFF^{F444W} - RFF^{F200W} = 0.2 - 11.6$. This is further evidence of the dust obscuration at shorter wavelengths in the SMGs, resulting in deviations from a simple light profile. This comparison suggests the SMGs have more complex morphologies at bluer wavelengths, which is likely to be linked to their intense star formation rates and the presence of highly structured dust in the SMGs, attenuating the shorter wavelength light.

To identify the physical mechanism driving the increase in structured emission identified in the SMGs (as quantified by the RFF and M_{20}) as a function of wavelength, in Figure 9 we compare the difference in morphological parameters measured between the F444W and F200W NIRCam bands for the SMGs and field galaxies. In Figure 9a we compare the dust content, as quantified by the A_V from SED fitting (Section 3.2), with $M_{20}^{F444W} - M_{20}^{F200W}$. As shown in Figure 3, the field galaxies have significantly lower A_V and less morphological variation with wavelength, with a median $M_{20}^{F444W} - M_{20}^{F200W} = 0.06 \pm 0.01$. The SMGs on the other hand, with higher A_V indicate a greater disparity between the F200W and F444W light distribution with a median value of $M_{20}^{F444W} - M_{20}^{F200W} = 0.34 \pm 0.04$. To quantify the trend between A_V and $M_{20}^{F444W} - M_{20}^{F200W}$ we perform an ODR fit to the running median shown in Figure 9 of the form,

$$A_V = A_{V,0} + \alpha(M_{20}^{F444W} - M_{20}^{F200W}), \quad (4)$$

We determine for the SMGs best-fit parameters of $\alpha = -1.0 \pm 0.3$ and $A_{V,0} = 3.1 \pm 0.1$, indicating a strong negative correlation for the SMGs, whereby more dust obscured (higher A_V) SMGs, have a more negative $M_{20}^{F444W} - M_{20}^{F200W}$, indicating less concentrated light profiles in the F200W band compared to the F444W.

To analyse the connection to other morphological parameters, in Figures 9b & d we plot $RFF^{F444W} - RFF^{F200W}$ against the difference in Asymmetry ($A^{F444W} - A^{F200W}$) and $M_{20}^{F444W} - M_{20}^{F200W}$, whilst in Figure 9c we compare the difference in Concentration ($C^{F444W} - C^{F200W}$) with $M_{20}^{F444W} - M_{20}^{F200W}$. All three relations indicate that on average the SMGs in the F200W band are more asymmetric and less concentrated, with more inhomogeneous light distributions leading to larger residuals to a single Sérsic fit at 2μm as compared to their 4μm morphologies.

4.3. Does structured dust drive the distinction between field and SMGs?

The morphological properties of the SMGs in the NIRCam F444W band are comparable to the field galaxies, with similar sizes at a fixed mass, slightly lower Sérsic indices and higher asymmetry (Figure 6). The F444W filter traces the rest-frame near-infrared ($\approx 1\mu m$) out to $z \sim 3.5$, and thus is less affected by dust obscuration and recent star formation than shorter bands

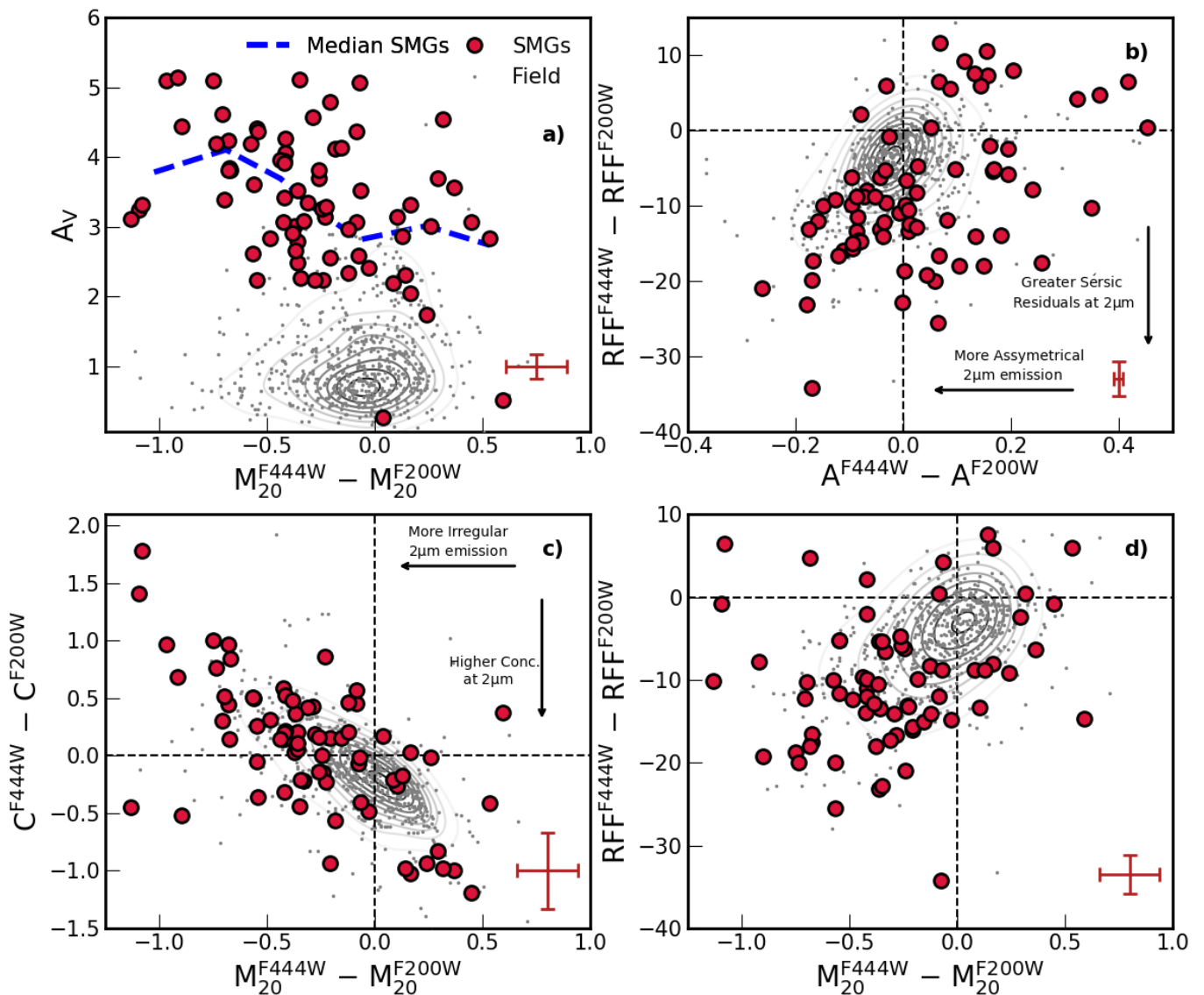Fig. 9: A comparison of the 2µm and 4µm morphological properties of the SMGs and field galaxies. We compare the difference in M_{20} parameter between the F444W and F200W bands ($M_{20}^{F444W} - M_{20}^{F200W}$) with dust attenuation (A_V) in panel *a)*. In panel *b)*, we further compare the difference in RFF between the F444W and F200W bands ($RFF^{F444W} - RFF^{F200W}$) with the difference in Asymmetry ($A^{F444W} - A^{F200W}$). Finally we plot the difference in M_{20} between F444W and F200W ($M_{20}^{F444W} - M_{20}^{F200W}$) with the difference in Concentration ($C^{F444W} - C^{F200W}$) (panel *c)*) and the difference in RFF (panel *d)*). All four panels indicate the SMGs are much more structured than the field population, with less uniform light distributions in the F200W compared to the F444W band, in contrast, the field galaxies show minimal wavelength variation.

in most of our sample. A greater difference between SMGs and field galaxies is identified at bluer wavelengths.

By investigating the variation M_{20} parameter and RFF between the NIRCam F444W band ($\lambda_{rest} \approx 1\mu m$) and F200W band ($\lambda_{rest} \approx 0.5\mu m$), Figures 8 and 9 highlight that the SMGs have more structured light profiles at shorter wavelengths, that results in larger residuals to single Sérsic fits of the light distribution. This morphological variation with wavelength was also highlighted by Chen et al. (2016) for SMGs and Nedkova et al. (2024) for SFGs, identifying that the most massive ($M_* \gtrsim 10^{10} M_\odot$) disc galaxies in their sample at $0.5 < z < 3$ have larger half-light radii in the rest-frame ultra-violet than optical, which they attribute to the significant dust attenuation in the central regions of the galaxies compared to the outskirts. A similar connection between with inferred galaxy morphology and dust content was identified in the Illustris – The Next Generation (TNG50; Pillepich et al. 2019) simulation by Popping et al. (2022). They suggested that the observed *H*-band to 870µm size ratio increases towards higher redshift (hence bluer rest-frame sampling) due to dust attenuating the central regions of galaxies, resulting in larger half-light radii in the *H*-band. The impact of dust on size measurements has also been quantified in the First Light And Reionisation Epoch Simulations (FLARES; Lovell et al. 2021; Vijayan et al. 2021), where intrinsically massive compact galaxies appear significantly more extended when the effects of dust are taken into account (Roper et al. 2022, 2023).

To isolate the contribution of dust to the SMGs morphological evolution as a function of wavelength, we examine
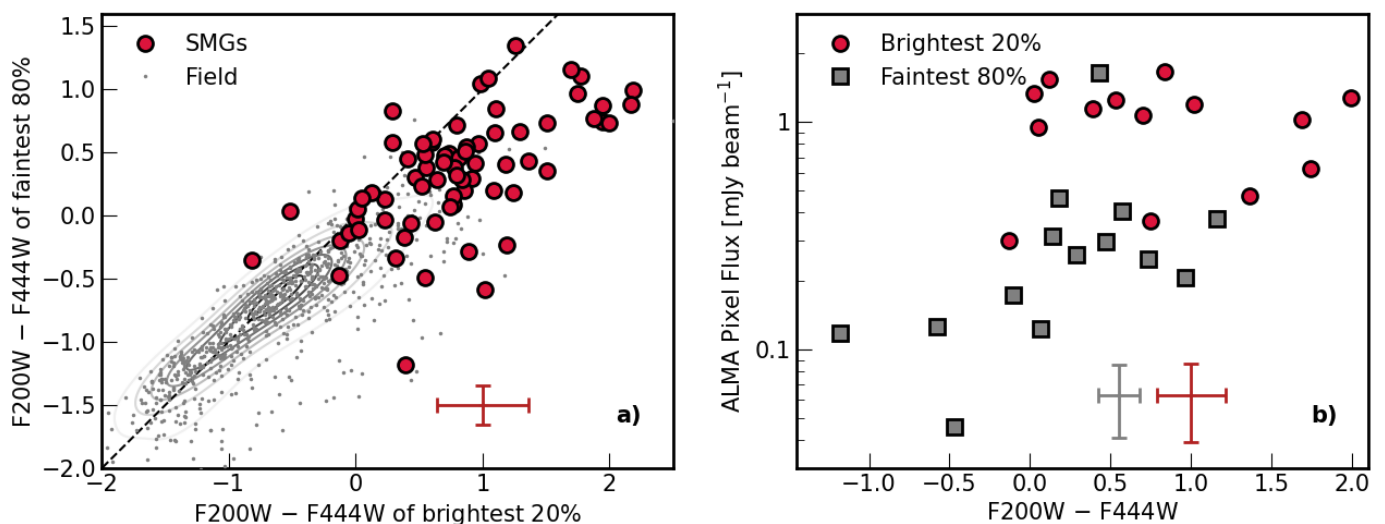
Fig. 10: *a)* We plot the average F200W − F444W colour of the faintest pixels (below 80th percentile of flux) inside $0\overset{''}{.}5$ elliptical apertures in the F444W image for the SMGs and field galaxies, as a function of the average colour for the top 20 per cent brightest F444W pixels. The field galaxies exhibit almost uniform colours between faint and bright regions, with a small offset to the equality line of 0.12 ± 0.03 mag (in the sense that the brightest pixels are redder), whilst the SMGs are both generally redder in fainter regions and significantly redder (1.11 ± 0.09 mag) in their brightest regions. In panel *b)* we show the average F200W − F444W colour of the "Brightest 20%" and "Faintest 80%" pixels as a function of ALMA pixel brightness. The brightest regions in the near-infrared (NIRCam F444W), which have the reddest F200W − F444W colour, correspond to the brightest regions in the far-infrared (ALMA 870μm).

the F200W − F444W pixel colours. In particular, given the $M_{20}^{\text{F444W}} - M_{20}^{\text{F200W}}$ parameter indicates the greatest morphological difference between field galaxies and SMGs, we calculate the average colour of the brightest 20 percent of pixels in the F444W image inside the $0\overset{''}{.}5$ elliptical apertures of each galaxy (Section 3.2). In Figure 10a, for both SMGs and field galaxies, we compare this "Brightest 20%" colour with the average colour of the fainter regions inside the same aperture ('Faintest 80%' F200W − F444W). Galaxies exhibiting no strong colour gradients between bright and faint regions will have consistent "Brightest 20%" and "Faintest 80%" colours, lying close to the one-to-one line. The majority of the field galaxies, as shown in Figure 10a, fall into this regime, with on average the brightest regions of the field galaxies being 0.12 ± 0.03 mag, redder than the faintest.

For the SMGs, the F200W − F444W pixel colour of the fainter regions that comprise the bulk of the galaxies ("Faintest 80%") indicate on average redder colours, with a median colour of 0.4 ± 0.06 mag compared to -0.74 ± 0.02 mag for the field galaxies. For the "Brightest 20%" pixel colour, the SMGs indicate significantly redder colours with a median value of 0.77 ± 0.06 mag compared to -0.66 ± 0.02 mag for the field galaxies. To understand whether the reddest (and brightest) regions of the SMGs are physically associated with the dust content, and thus 870μm emission, of the galaxies we analyse high-resolution ALMA 870μm observations for a sub-sample of 15 SMGs with ALMA maps from Gullberg et al. (2019), having a synthesised beam of FWHM $\leq 0\overset{''}{.}2$.

We resample the ALMA maps to match the $0\overset{''}{.}04$ pixel scale of the JWST NIRCam F444W imaging. We then extract the same average "Brightest 20%" and "Faintest 80%" F200W − F444W pixel colour as before for each SMG. In Figure 10b, we correlate this pixel colour with the ALMA 870μm pixel brightness for the "Brightest 20%" and "Faintest 80%" pixels. We identify a strong correlation between F200W − F444W pixel colour and

870μm surface brightness, demonstrating that the reddest colour that originates from the brightest regions of the SMGs, is physically associated with the brightest regions of the 870μm emission and thus high dust column density regions.

4.3.1. Dust Content and the Interstellar Medium of SMGs

A high dust column density in the SMGs, as Figure 10 implies, would suggest that the optical to near-infrared emission of the SMGs is strongly attenuated. Consequently, physical properties estimated from the SED fitting (e.g. A_V) may be uncertain due to heavily obscured regions of the galaxies being undetected. We can derive the expected *V*-band extinction (A_V) given the median dust mass ($\log_{10}(M_d[M_\odot]) = 8.9 \pm 0.2$) derived from SED fitting (Sec 3.2) and compare this to the A_V derived by MAGPHYS from fitting the optical to near-infrared SED. As shown by Güver & Özel (2009), the column density of hydrogen (in cm^{-2}) can be approximated from the A_V (in mag) as follows,

$$N_H = 2.21 \times 10^{21} \, A_V \qquad (5)$$

Adopting a dust-to-gas ratio of $\delta = 63 \pm 7$ as derived by (Birkin et al. 2021), for SMGs with typical metallicity, star-formation rates and stellar masses (e.g., Rémy-Ruyer et al. 2014) and assuming the F444W half-light radius provides an upper-limit on the physical extent of the dust region, we obtain a lower-limit on the median *V*-band dust attenuation of $A_V = 110 \pm 20$. This is two orders of magnitude higher than that derived from the SED fitting of SMGs with the median MAGPHYS estimated value of $A_V = 3.4 \pm 0.16$. For the A_V derived from MAGPHYS, which constrains the dust obscuration of the visible stars, an energy balance calculation is assumed such that far-infrared emission is broadly consistent with the absorbed stellar light of the system (Battisti et al. 2019). This assumption assumes the UV/optical and far-infrared emission are co-spatial and well mixed however, inaccuracies can arise as detectable optical emission does not encode

information about the ongoing obscured star formation of the galaxy (e.g., Simpson et al. 2017; Buat et al. 2019; Haskell et al. 2023; Killi et al. 2024). In the derivation of A_V from the dust mass, which defines the dust obscuration of the deepest regions of the clouds, we have estimated a Compton thick HI column where the dust is uniformly distributed in a smooth "disk-like" component as identified in the high-resolution ALMA studies of SMGs (e.g., Hodge et al. 2016; Gullberg et al. 2019). However, numerical studies suggest that the star dust geometry plays a crucial role in determining the attenuation curve of the galaxies (e.g., Inoue 2005; Sachdeva & Nath 2022; Vijayan et al. 2024) as well as the metallicity of the interstellar medium (e.g., Shivaei et al. 2020).

With such high levels of inferred dust obscuration, and intense star formation rates, the question remains what are underlying interstellar medium conditions that give rise to these extreme physical properties in the SMGs. To infer the properties of the interstellar medium we compare the surface density of star formation, (Σ_{SFR}), to the gas surface density (Σ_{gas}) i.e., the density of fuel for star formation. For the SMGs, we use the gas mass derived above, the star-formation rate from MAGPHYS and the F444W half-light radius as a conservative estimate of the physical extent of the gas content. For the field sample, we use the MAGPHYS derived dust masses with a median value of $\log_{10}(M_d[M_\odot]) = 7.7 \pm 0.1$, which are consistent with the dust mass inferred from converting the $S_{870\mu m}$ limit, derived from stacks in S2CLS UDS 870μm map (Geach et al. 2017), to a dust mass using the $S_{870\mu m}$ to dust mass relation defined in Dudzevičiūtė et al. (2020). Adopting the metallicity-dependent dust-to-gas ratio from Tacconi et al. (2018) for massive star-forming galaxies and following the mass metallicity relation defined in Genzel et al. (2015), we derive a median dust-to-gas ratio of $\delta = 163 \pm 32$ which equates to a median gas mass of $\log_{10}(M_g[M_\odot]) = 9.8 \pm 0.1$ for the field galaxies.

Combining this gas mass estimate for the field with the MAGPHYS derived star-formation rates and F444W half-light radius, in Figure 11 we show the relation between Σ_{SFR} and Σ_{gas} for both the field sample and SMGs. Given the higher star-formation rates and dust masses of the SMGs (Figure 3) and their comparable sizes in the F444W band to the field galaxies (Figure 6), the SMGs have considerably higher star-formation rate surface density and gas surface density. However, both field galaxies and SMGs have comparable time scales for star formation, lying close to the 0.1 Gyr star formation time scale.

By estimating the Toomre Q parameter (Toomre 1964) we can place constraints on the interstellar medium properties of the galaxies, in particular on the stability of the gas disk. The Toomre Q is defined as,

$$Q = \frac{\sigma \kappa}{\pi G \Sigma_{gas}} \quad (6)$$

where σ is the radial velocity dispersion, κ is the epicyclic frequency, for which we adopt $\kappa = \sqrt{2}V/R$ appropriate for a galaxy with a flat rotation curve and Σ_{gas} is the gas surface density. For the rotation velocity and velocity dispersion, we adopt the median values from Birkin et al. (2023), for a sample 31 SMGs in the AS2UDS survey, with comparable median redshift and stellar mass to our sample ($z \sim 1.3 - 2.6$, $\log_{10}(M_*[M_\odot]) = 11.11 \pm 0.06$). Birkin et al. (2023) derive a median rotation velocity and velocity dispersion of $V_{circ} = 230 \pm 20$ km s^{-1} and $\sigma = 87 \pm 6$ km s^{-1}.

Adopting the F444W half-light radius as an estimate of the extent of the gas disk, we can derive the gas-surface density required for a quasi-stable gas disk, identifying a threshold value
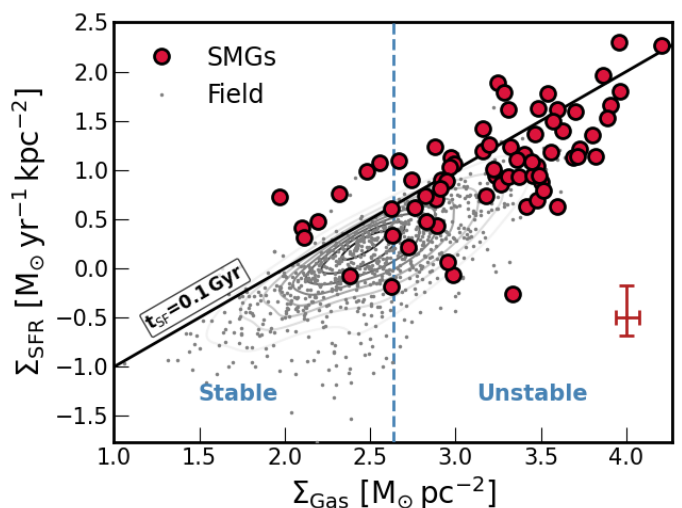

Fig. 11: The relation between star-formation rate surface density and gas surface density for the field sample (grey points and contour) and SMGs (red circles). We indicate a constant star-formation time scale of 0.1 Gyr with the black line. Adopting the typical rotation velocity and velocity dispersion from Birkin et al. (2023) derived for a sample of AS2UDS SMGs, we define the boundary between stable ($Q > 1$) and unstable ($Q < 1$) gas disks. The majority of the SMGs indicate unstable gas disks with a median Toomre Q parameter of $Q = 0.47 \pm 0.06$.

of $\log_{10}(\Sigma_{gas}) = 2.64 \pm 0.05$ M$_\odot$pc^{-2}. This implies the gas disk is unstable to collapse ($Q < 1$) for gas-surface densities higher than this value. We estimate that the majority of the SMGs lie in this region of "instability" with a median Toomre Q parameter of $Q = 0.47 \pm 0.06$. Given the F444W half-light radius provides a lower limit on the extent of gas disk, to generate a quasi-stable interstellar medium in the SMGs, we require larger rotation velocity or velocity dispersion. Requiring that the gas disk is quasi-stable i.e $Q \geq 1$, we derive a lower limit on the radial velocity dispersion required for stability. Adopting the rotation velocity from Birkin et al. (2023), we derive a median velocity dispersion for stability of $\sigma_{stable} \geq 200 \pm 30$ km s^{-1} which is significantly larger than that derived for ionised gas in previous studies of high redshift SMGs or U/LIRGS (e.g. Hogan et al. 2021; Birkin et al. 2023; Amvrosiadis et al. 2024), suggesting that the gaseous disks of the SMGs in our sample are significantly unstable to gravitational collapse.

4.4. Implications for the nature of SMGs

The SMG and field samples share several characteristics. By construction, they have similar number densities as a function of redshift and specific star formation rates. Furthermore, we have demonstrated they have similar rates of mergers and signatures of disturbance, with comparable rest-frame near-infrared axis ratios and mass normalised stellar continuum (F444W) sizes. This suggests that the major structural components in both populations comprise (randomly orientated) disks that broadly follow the size-mass relation for disk galaxies at $z \sim 2 - 3$. The similarity in the merger fractions for the SMGs and field is consistent with the theoretical investigation of SMGs in the EAGLE simulation by McAlpine et al. (2019), who concluded that there was no difference in merger statistics of the SMGs and the general population, instead most galaxies at these redshifts were undergoing minor or major mergers.

However, there are several distinctions between the SMGs and less-active field galaxies. The dust-mass-selected SMGs have much higher A_V and asymmetry, and they show stronger variations in their morphologies at bluer wavelengths, indicating the presence of structured and centrally concentrated dust. Moreover, the field has an average Sérsic index of $n \sim 1.9$, indicating the potential presence of a bulge component in these systems. The SMGs have consistently lower Sérsic index, with a median of $n \sim 1.1$, indicating they are nearly pure exponential disks or that any bulge component if present is invisible at rest-frame $\sim 1\mu$m. Either of these interpretations suggests that any bulge component in the SMGs is of low mass compared to the disk or is likely to be young and so only recently formed.

We also infer more than an order of magnitude higher molecular gas surface densities for the SMGs than the field. These differences suggest that one possible cause for a distinction between SMGs and less active galaxies arises from the less developed bulge components present in the SMGs. Consequently, their gas disks are more sensitive to developing low-order disk instabilities, including $m = 1$ bars (e.g., Marinova & Jogee 2007; Pettitt & Wadsley 2018). These instabilities can either be triggered by external perturbations from major or minor mergers or tidal interactions, or from secular instabilities in the dense gas disks. These structures, as predicted by theoretical models (e.g., Fragkoudi et al. 2021; Bland-Hawthorn et al. 2023) and identified in recent studies of individual high-redshift SMGs (e.g., Smail et al. 2023; Amvrosiadis et al. 2024) serve to funnel gas from the dense gas disk into the central regions of the galaxies, driving a central starburst that creates both the compact submillimetre emission we see and the corresponding highly obscured central regions of these systems.

5. Conclusions

We present a multi-wavelength morphological analysis of a complete sample of SMGs from the AS2UDS and AS2COSMOS surveys (Stach et al. 2019; Simpson et al. 2020) with $>4.5\sigma$ ALMA 870μm detections and positions. Utilising the public JWST/NIRCam and MIRI imaging from the PRIMER survey, we build a sample of 80 SMGs, determining their multi-wavelength properties through a SED and morphological analysis. We further define a redshift and specific star-formation rate matched sample of less active and more typical K-band selected star-forming field galaxies in the UDS field and analyse the differences between the two populations. Our main conclusions are:

- We identify F444W counterparts to 99% (87/88) of the ALMA-detected SMGs at $m_{F444W} = 20.3 - 23.1$, showing that the vast majority of galaxies hosting intense, dusty starbursts are detectable by JWST. Of those 87, we identify two SMGs with morphologies indicative of strong galaxy-galaxy lensing, a rate consistent with early estimates. Removing these lensed SMGs, in addition to a further six sources with partial NIRCam coverage, one spurious ALMA source and deblending one ALMA source into two NIRCam sources results in a final sample of 80 SMGs which have clear NIRCam counterparts.
- The SMGs have significantly redder F200W−F444W and F444W−F770W colours than the field sample, with comparable F090W−F200W and F770W−F1800W. We identify $24 \pm 5\%$ of the field galaxies and $3 \pm 1\%$ of the SMGs show red F770W−F1800W combined with blue F444W−F770W colours, potentially indicating the presence of AGN or a strong 6.2μm PAH feature present in the F1800W filter at $z \sim 1.9$.

- From visually inspecting the F277W/F356W/F444W colour images of the SMGs we identify $20 \pm 5\%$ as candidate major mergers, a further $40 \pm 10\%$ as potential minor mergers and the remaining 40% are isolated systems with no obvious neighbours on $\simeq 20 - 30$ kpc (projected) scales. We find no dependence of the visual classification on far-infrared luminosity. These statistics are very similar to the rates determined for the field sample and demonstrate that the majority of SMGs are not ongoing major mergers, although mergers (major or minor) and disturbed appearances are common in both the SMGs and the less active field population at these redshifts.
- Through a parametric and non-parametric morphological analysis, we determine the SMGs and field galaxies exhibit similar rest-frame near-infrared axis ratios and mass-normalised half-light radii with $R_h = 2.7 \pm 0.2$ kpc and $R_h = 3.1 \pm 0.1$ kpc for the SMGs and field respectively, lying slightly below the rest-frame optical mass size relation at their epoch.
- The SMG and field populations are more distinct in their detailed morphologies in terms of Sérsic index (n) and Asymmetry (A) in the F444W band, with the SMGs having lower Sérsic indices and higher Asymmetry ($n_{F444W} = 1.1 \pm 0.1$, $A_{F444W} = 0.13 \pm 0.02$) compared to the field galaxies ($n_{F444W} = 1.9 \pm 0.1$, $A_{F444W} = 0.08 \pm 0.01$).
- A similar disparity between the SMGs and typical star-forming galaxies is seen in the variation of their morphologies as a function of wavelength. The size of the SMGs declines more rapidly at longer wavelengths than field galaxies ($\delta(R_h/R_{1\mu m})/\delta\lambda = -0.60 \pm 0.09$ versus $\delta(R_h/R_{1\mu m})/\delta\lambda = -0.15 \pm 0.07$). Furthermore the SMGs exhibit lower Sérsic indices at all wavelengths with $n_0 = 1.0 \pm 0.04$ compared to the field galaxies ($n_0 = 1.51 \pm 0.10$). The SMGs also exhibit a greater scatter in morphology at bluer wavelengths that is likely to originate from both their structured dust content and higher star formation rates compared to the field galaxies.
- A comparison of the Gini$-M_{20}$ relation for the SMGs and field sample at 2μm (rest-frame V-band) and 4μm (rest-frame z-band) underlines the variation in morphology as a function of wavelength, with 40% of the SMGs lying in the merger region (as defined at $z = 0$ in the rest-frame R-band) at 2μm whilst only 8% do so at 4μm.
- We establish that the variation of the M_{20} and residual flux fraction (RFF) parameter between the F200W and F444W NIRCam bands provides a clear distinction between SMGs and field galaxies with a median value of $RFF^{F444W} - RFF^{F200W} = -10.0 \pm 1.2$ for the SMGs whilst for the field galaxies the median is $RFF^{F444W} - RFF^{F200W} = -4.6 \pm 0.3$. This demonstrates that the F200W light-distributions of the SMGs are more structured, relative to their appearance in F444W, resulting in greater residuals and M_{20} values compared to the field galaxies.
- To identify the cause of this behaviour, we explore the internal F200W − F444W colour gradients of the galaxies. The SMGs are generally redder than the field galaxies as expected, but crucially the brightest regions in F444W are 1.1 ± 0.1 magnitudes redder than than the fainter regions (this offset is three times larger than that seen in the field population) indicating the presence of centrally concentrated starbursts. We further determine the brightest and reddest regions of the SMGs in the NIRCam imaging correspond to the highest surface brightness emission at 870μm seen by

ALMA, indicating a strong connection between the colour and the dust content of the galaxy.

- To understand the physical origin of the difference in morphologies between the SMGs and the field galaxies, we assume a representative gas-to-dust ratio to define the relation between star-formation rate surface density and gas surface density, suggesting that the SMGs have significantly higher gas surface densities than field galaxies. The SMGs on average fall in the unstable ($Q < 1$) regime with a median Toomre Q parameter of $Q = 0.47 \pm 0.06$.

Our analysis indicates that SMGs and typical star-forming galaxies appear morphologically distinct in the rest-frame optical due to the higher dust content of the SMGs, which preferentially influences the central regions of the galaxies. Whilst at longer wavelengths, sampling the rest-frame near-infrared, the SMGs and less active field galaxies show more similar mass-normalised sizes, although the SMGs exhibit lower Sérsic parameters, suggesting they have weaker bulge components. Both the SMGs and field control samples have comparable rates of candidate mergers and undisturbed galaxies, suggesting that mergers are not a unique driver of the activity in SMGs. Instead, we suggest that the higher gas surface densities and weaker bulge components, coupled with the perturbations caused by either major or minor mergers, as well as secular processes, lead to correspondingly more intense star-formation activity in the SMGs, compared to the field. Thus the defining characteristic of SMGs maybe their massive and gas-rich nature, coupled with relatively underdeveloped bulge components and correspondingly low black hole masses.

Software

Astropy (Astropy Collaboration et al. 2013, 2018), Photutils (Bradley et al. 2022), Source Extractor (Bertin & Arnouts 1996b) SEP (Barbary et al. 2016) Eazy-py (Brammer & Matharu 2021) GriZli (Brammer et al. 2022) GalfitM (Häußler et al. 2013) Statmorph (Rodriguez-Gomez et al. 2019) Topcat (Taylor 2005)

References

Abraham R. G., van den Bergh S., Nair P., 2003, ApJ, 588, 218
Aguirre P., Baker A. J., Menanteau F., Lutz D., Tacconi L. J., 2013, ApJ, 768, 164
Alaghband-Zadeh S., et al., 2012, MNRAS, 424, 2232
Alberts S., et al., 2013, MNRAS, 431, 194
Amvrosiadis A., et al., 2018, MNRAS, 475, 4939
Amvrosiadis A., et al., 2023, arXiv e-prints, p. arXiv:2312.08959
Amvrosiadis A., et al., 2024, arXiv e-prints, p. arXiv:2404.01918
An F. X., et al., 2018, ApJ, 862, 101
Aniano G., et al., 2020, ApJ, 889, 150
Astropy Collaboration et al., 2013, A&A, 558, A33
Astropy Collaboration et al., 2018, AJ, 156, 123
Barbary K., Boone K., McCully C., Craig M., Deil C., Rose B., 2016, Kbarbary/Sep: V1.0.0, Zenodo, doi:10.5281/zenodo.159035
Battisti A. J., et al., 2019, ApJ, 882, 61
Baugh C. M., Lacey C. G., Frenk C. S., Granato G. L., Silva L., Bressan A., Benson A. J., Cole S., 2005, MNRAS, 356, 1191
Bendo G. J., et al., 2023, MNRAS, 522, 2995
Bertin E., Arnouts S., 1996a, A&AS, 117, 393
Bertin E., Arnouts S., 1996b, A&AS, 117, 393
Birkin J. E., et al., 2021, MNRAS, 501, 3926
Birkin J. E., et al., 2023, arXiv e-prints, p. arXiv:2301.05720
Bland-Hawthorn J., Tepper-Garcia T., Agertz O., Freeman K., 2023, ApJ, 947, 80
Bouwens R., et al., 2020, ApJ, 902, 112
Bradley L., et al., 2022, astropy/photutils: 1.5.0, Zenodo, doi:10.5281/zenodo.6825092
Brammer G., Matharu J., 2021, gbrammer/grizli: Release 2021, Zenodo, doi:10.5281/zenodo.5012699
Brammer G., Strait V., Matharu J., Momcheva I., 2022, grizli, Zenodo, doi:10.5281/zenodo.6672538
Buat V., Ciesla L., Boquien M., Małek K., Burgarella D., 2019, A&A, 632, A79
Calistro Rivera G., et al., 2018, ApJ, 863, 56
Casey C. M., et al., 2013, MNRAS, 436, 1919
Chabrier G., 2003, PASP, 115, 763
Chapman S. C., Smail I., Ivison R. J., Blain A. W., 2002, MNRAS, 335, L17
Chapman S. C., Windhorst R., Odewahn S., Yan H., Conselice C., 2003, ApJ, 599, 92
Chapman S. C., Smail I., Windhorst R., Muxlow T., Ivison R. J., 2004, ApJ, 611, 732
Chen C.-C., et al., 2015, ApJ, 799, 194
Chen C.-C., et al., 2016, ApJ, 831, 91
Chen C.-C., et al., 2017, ApJ, 846, 108
Chen C.-C., et al., 2020, A&A, 635, A119
Chen C.-C., et al., 2022, ApJ, 939, L7
Cheng C., et al., 2023, ApJ, 942, L19
Cochrane R. K., et al., 2021, MNRAS, 503, 2622
Cochrane R. K., Anglés-Alcázar D., Cullen F., Hayward C. C., 2023, arXiv e-prints, p. arXiv:2310.08829
Conselice C. J., Chapman S. C., Windhorst R. A., 2003, ApJ, 596, L5
Cowie L. L., González-López J., Barger A. J., Bauer F. E., Hsu L. Y., Wang W. H., 2018, ApJ, 865, 106
Downes A. J. B., Peacock J. A., Savage A., Carrie D. R., 1986, MNRAS, 218, 31
Draine B. T., et al., 2007, ApJ, 663, 866
Drew P. M., Casey C. M., Cooray A., Whitaker K. E., 2020, ApJ, 892, 104
Dudzevičiūtė U., et al., 2020, MNRAS, 494, 3828
Dunlop J. S., et al., 2017, MNRAS, 466, 861
Dunlop J. S., et al., 2021, PRIMER: Public Release IMaging for Extragalactic Research, JWST Proposal. Cycle 1, ID. #1837
Engel H., et al., 2010, ApJ, 724, 233

Faisst A. L., et al., 2024, arXiv e-prints, p. arXiv:2405.09619
Farrah D., et al., 2001, MNRAS, 326, 1333
Fazio G. G., et al., 2004, ApJS, 154, 10
Fragkoudi F., Grand R. J. J., Pakmor R., Springel V., White S. D. M., Marinacci F., Gomez F. A., Navarro J. F., 2021, A&A, 650, L16
Fruchter A. S., Hook R. N., 2002, PASP, 114, 144
Fujimoto S., Ouchi M., Shibuya T., Nagai H., 2017, ApJ, 850, 83
Gaia Collaboration et al., 2021, A&A, 649, A1
Gardner J. P., et al., 2023, PASP, 135, 068001
Geach J. E., et al., 2017, MNRAS, 465, 1789
Genzel R., et al., 2015, ApJ, 800, 20
Gillman S., et al., 2023, A&A, 676, A26
Gómez-Guijarro C., et al., 2018, ApJ, 856, 121
Greve T. R., et al., 2005, MNRAS, 359, 1165
Grogin N. A., et al., 2011, ApJS, 197, 35
Gullberg B., et al., 2019, MNRAS, 490, 4956
Guo Y., et al., 2023, ApJ, 945, L10
Güver T., Özel F., 2009, MNRAS, 400, 2050
Haskell P., Smith D. J. B., Cochrane R. K., Hayward C. C., Anglés-Alcázar D., 2023, MNRAS, 525, 1535
Häußler B., et al., 2013, MNRAS, 430, 330
Hayward C. C., Narayanan D., Kereš D., Jonsson P., Hopkins P. F., Cox T. J., Hernquist L., 2013, MNRAS, 428, 2529
Hodge J. A., da Cunha E., 2020, Royal Society Open Science, 7, 200556
Hodge J. A., Carilli C. L., Walter F., de Blok W. J. G., Riechers D., Daddi E., Lentati L., 2012, ApJ, 760, 11
Hodge J. A., et al., 2013, ApJ, 768, 91
Hodge J. A., et al., 2016, ApJ, 833, 103
Hodge J. A., et al., 2019, ApJ, 876, 130
Hogan L., Rigopoulou D., Magdis G. E., Pereira-Santaella M., García-Bernete I., Thatte N., Grisdale K., Huang J. S., 2021, MNRAS, 503, 5329
Hopkins P. F., Younger J. D., Hayward C. C., Narayanan D., Hernquist L., 2010, MNRAS, 402, 1693
Hoyos C., et al., 2011, MNRAS, 411, 2439
Hoyos C., et al., 2012, MNRAS, 419, 2703
Hwang Y.-H., et al., 2021, ApJ, 913, 6
Ikarashi S., et al., 2015, ApJ, 810, 133
Ikarashi S., Ivison R. J., Cowley W. I., Kohno K., 2022, A&A, 659, A154
Inoue A. K., 2005, MNRAS, 359, 171
Ivison R. J., et al., 2002, MNRAS, 337, 1
Ivison R. J., et al., 2004, ApJS, 154, 124
Kamieneski P. S., et al., 2023, ApJ, 955, 91
Kartaltepe J. S., et al., 2010, ApJ, 721, 98
Kartaltepe J. S., et al., 2023, ApJ, 946, L15
Killi M., et al., 2024, arXiv e-prints, p. arXiv:2402.07982
Kirkpatrick A., et al., 2013, ApJ, 763, 123
Kirkpatrick A., et al., 2017, ApJ, 849, 111
Kokorev V., et al., 2022, ApJS, 263, 38
Kokorev V., et al., 2023, A&A, 677, A172
Kron R. G., 1980, ApJS, 43, 305
Lang P., et al., 2019, ApJ, 879, 54
Lawrence A., et al., 2007, MNRAS, 379, 1599
Lelli F., Di Teodoro E. M., Fraternali F., Man A. W. S., Zhang Z.-Y., De Breuck C., Davis T. A., Maiolino R., 2021, Science, 371, 713
Liang P., Dai Y. S., Huang J.-S., Cheng C., Yaru S., 2024, arXiv e-prints, p. arXiv:2405.06984
Ling C., Yan H., 2022, ApJ, 929, 40
Liu Z., et al., 2023, arXiv e-prints, p. arXiv:2311.14809

Long A. S., Casey C. M., del P. Lagos C., Lambrides E. L., Zavala J. A., Champagne J., Cooper O. R., Cooray A. R., 2023, ApJ, 953, 11
Lotz J. M., Primack J., Madau P., 2004, AJ, 128, 163
Lotz J. M., et al., 2008, ApJ, 672, 177
Lovell C. C., Vijayan A. P., Thomas P. A., Wilkins S. M., Barnes D. J., Irodotou D., Roper W., 2021, MNRAS, 500, 2127
Lower S., Narayanan D., Li Q., Davé R., 2023, ApJ, 950, 94
Magnelli B., et al., 2012, A&A, 539, A155
Marinova I., Jogee S., 2007, ApJ, 659, 1176
McAlpine S., et al., 2019, MNRAS, 488, 2440
McLure R. J., et al., 2018, MNRAS, 479, 25
Miettinen O., Delvecchio I., Smolčić V., Aravena M., Brisbin D., Karim A., 2017a, A&A, 602, L9
Miettinen O., et al., 2017b, A&A, 606, A17
Mitsuhashi I., et al., 2021, ApJ, 907, 122
Nedkova K. V., et al., 2024, arXiv e-prints, p. arXiv:2405.10908
Pandya V., et al., 2024, ApJ, 963, 54
Pearson J., et al., 2024, MNRAS, 527, 12044
Peng C. Y., Ho L. C., Impey C. D., Rix H.-W., 2010, AJ, 139, 2097
Perrin M. D., Sivaramakrishnan A., Lajoie C.-P., Elliott E., Pueyo L., Ravindranath S., Albert L., 2014, in Oschmann Jacobus M. J., Clampin M., Fazio G. G., MacEwen H. A., eds, Society of Photo-Optical Instrumentation Engineers (SPIE) Conference Series Vol. 9143, Space Telescopes and Instrumentation 2014: Optical, Infrared, and Millimeter Wave. p. 91433X, doi:10.1117/12.2056689
Pettitt A. R., Wadsley J. W., 2018, MNRAS, 474, 5645
Pillepich A., et al., 2019, MNRAS, 490, 3196
Polletta M., et al., 2024, arXiv e-prints, p. arXiv:2405.07986
Popping G., et al., 2022, MNRAS, 510, 3321
Price S. H., et al., 2023, arXiv e-prints, p. arXiv:2310.02500
Rémy-Ruyer A., et al., 2014, A&A, 563, A31
Ren J., et al., 2024, arXiv e-prints, p. arXiv:2404.16686
Rizzo F., Vegetti S., Fraternali F., Stacey H. R., Powell D., 2021, MNRAS, 507, 3952
Rodriguez-Gomez V., et al., 2019, MNRAS, 483, 4140
Roper W. J., Lovell C. C., Vijayan A. P., Marshall M. A., Irodotou D., Kuusisto J. K., Thomas P. A., Wilkins S. M., 2022, MNRAS, 514, 1921
Roper W. J., et al., 2023, MNRAS, 526, 6128
Rowlands K., et al., 2014, MNRAS, 441, 1017
Rujopakarn W., et al., 2023, ApJ, 948, L8
Sachdeva S., Nath B. B., 2022, MNRAS, 513, L63
Sanders D. B., Soifer B. T., Elias J. H., Madore B. F., Matthews K., Neugebauer G., Scoville N. Z., 1988, ApJ, 325, 74
Scoville N., et al., 2007, ApJS, 172, 1
Shivaei I., et al., 2020, ApJ, 899, 117
Shivaei I., et al., 2024, arXiv e-prints, p. arXiv:2402.07989
Simpson J. M., et al., 2014, ApJ, 788, 125
Simpson J. M., et al., 2015, ApJ, 807, 128
Simpson J. M., et al., 2017, ApJ, 839, 58
Simpson J. M., et al., 2019, ApJ, 880, 43
Simpson J. M., et al., 2020, MNRAS, 495, 3409
Smail I., Ivison R. J., Blain A. W., Kneib J. P., 1998, ApJ, 507, L21
Smail I., et al., 2021, MNRAS, 502, 3426
Smail I., et al., 2023, ApJ, 958, 36
Snyder G. F., et al., 2015, MNRAS, 454, 1886
Stach S. M., et al., 2019, MNRAS, 487, 4648
Suess K. A., et al., 2022, ApJ, 937, L33
Sun F., et al., 2024, ApJ, 961, 69
Swinbank A. M., et al., 2008, MNRAS, 391, 420
Swinbank A. M., et al., 2010, MNRAS, 405, 234

Swinbank A. M., et al., 2014, MNRAS, 438, 1267

Tacconi L. J., et al., 2008, ApJ, 680, 246

Tacconi L. J., et al., 2018, ApJ, 853, 179

Taylor M. B., 2005, in Shopbell P., Britton M., Ebert R., eds, Astronomical Society of the Pacific Conference Series Vol. 347, Astronomical Data Analysis Software and Systems XIV. p. 29

Toomre A., 1964, ApJ, 139, 1217

Vijayan A. P., Lovell C. C., Wilkins S. M., Thomas P. A., Barnes D. J., Irodotou D., Kuusisto J., Roper W. J., 2021, MNRAS, 501, 3289

Vijayan A. P., Thomas P. A., Lovell C. C., Wilkins S. M., Greve T. R., Irodotou D., Roper W. J., Seeyave L. T. C., 2024, MNRAS, 527, 7337

Ward E., et al., 2024, ApJ, 962, 176

Wardlow J. L., et al., 2011, MNRAS, 415, 1479

Wu Y., et al., 2023, ApJ, 942, L1

Yang G., et al., 2023, arXiv e-prints, p. arXiv:2307.14509

Yu S.-Y., Cheng C., Pan Y., Sun F., Li Y. A., 2023, A&A, 676, A74

Zavala J. A., et al., 2018, MNRAS, 475, 5585

da Cunha E., et al., 2015, ApJ, 806, 110

van der Wel A., et al., 2012, ApJS, 203, 24

van der Wel A., et al., 2024, ApJ, 960, 53

ORCIDs

Steven Gillman ⓘ 0000-0001-9885-4589

Ian Smail ⓘ 0000-0003-3037-257X

Bitten Gullberg ⓘ 0000-0002-4671-3036,

A. M. Swinbank ⓘ 0000-0003-1192-5837

Aswin P. Vijayan ⓘ 0000-0002-1905-4194,

Gabe Brammer ⓘ 0000-0003-2680-005X

Thomas R. Greve ⓘ 0000-0002-2554-1837

Omar Almaini ⓘ 0000-0001-9328-3991

Malte Brinch ⓘ 0000-0002-0245-6365

Chian-Chou Chen ⓘ 0000-0002-3805-0789

Wei-Hao Wang ⓘ 0000-0003-2588-1265

Yuichi Matsuda ⓘ 0000-0003-1747-2891

Fabian Walter ⓘ h0000-0003-4793-7880

Paul P. van der Werf ⓘ 0000-0001-5434-5942

Appendix A: SMG Properties

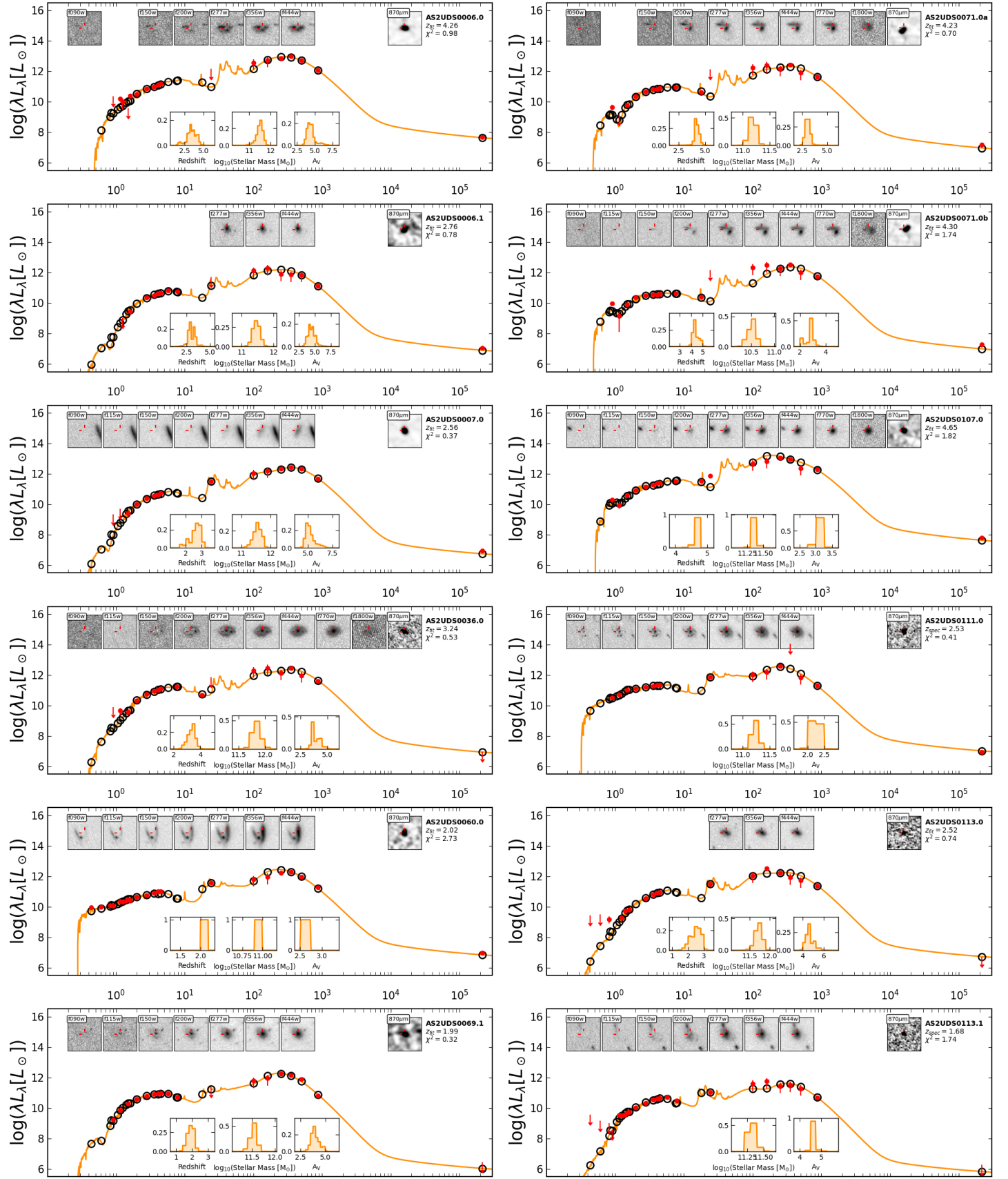The table summarising the SMG properties is available online only.

Appendix B: SEDs

Fig. .1: For each SMG we plot the multi-wavelength photometry (red points) and MAGPHYS derived SED fit (gold line), where arrows indicates the limits. Beneath each SED we show histograms of the MAGPHYS probability density functions of redshift, stellar mass and attenuation in *V*-band. We also display the JWST and ALMA 870μm imaging for each source, with the derived photometric redshift and reduced chi-squared of the fit in the top right corner.
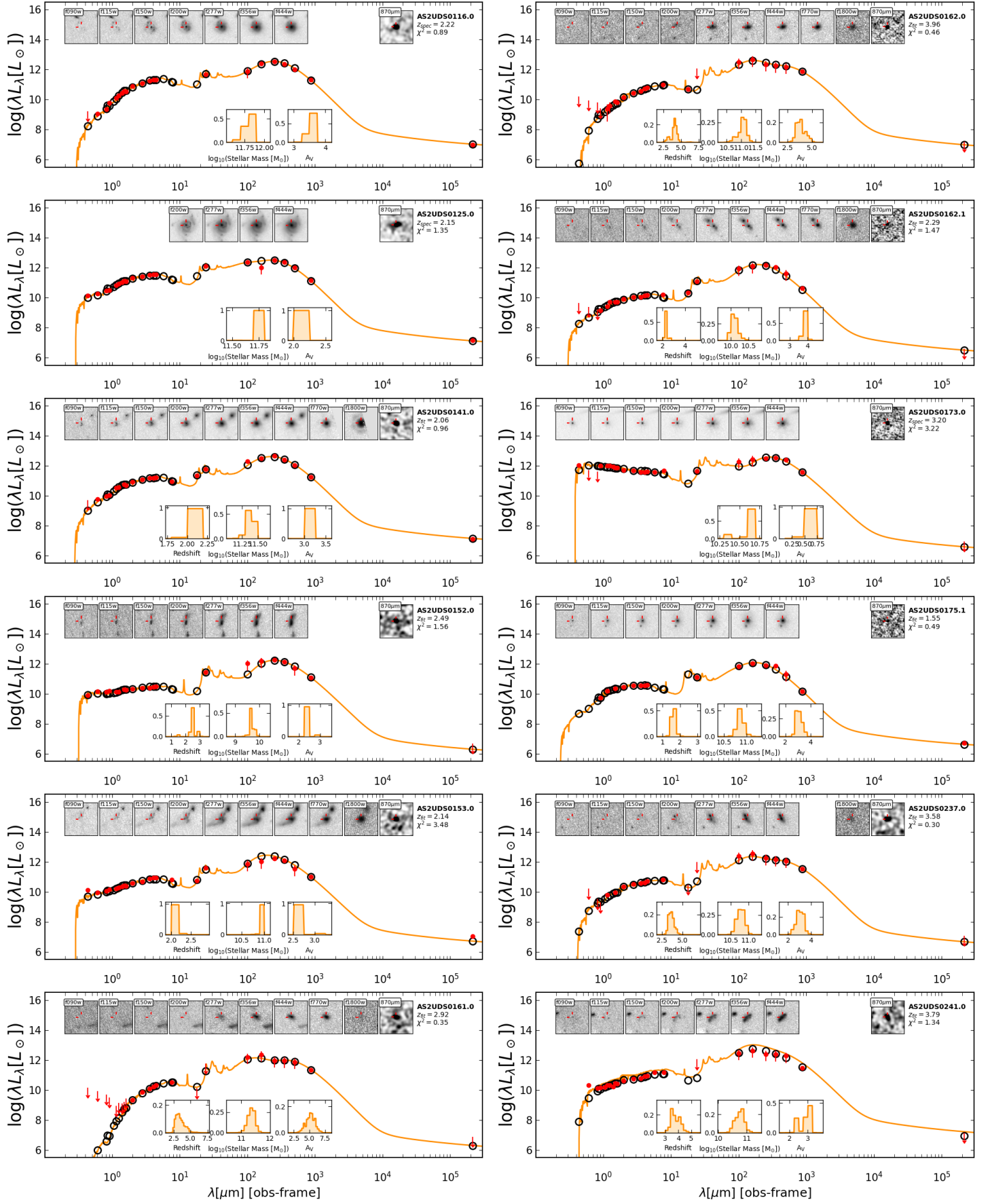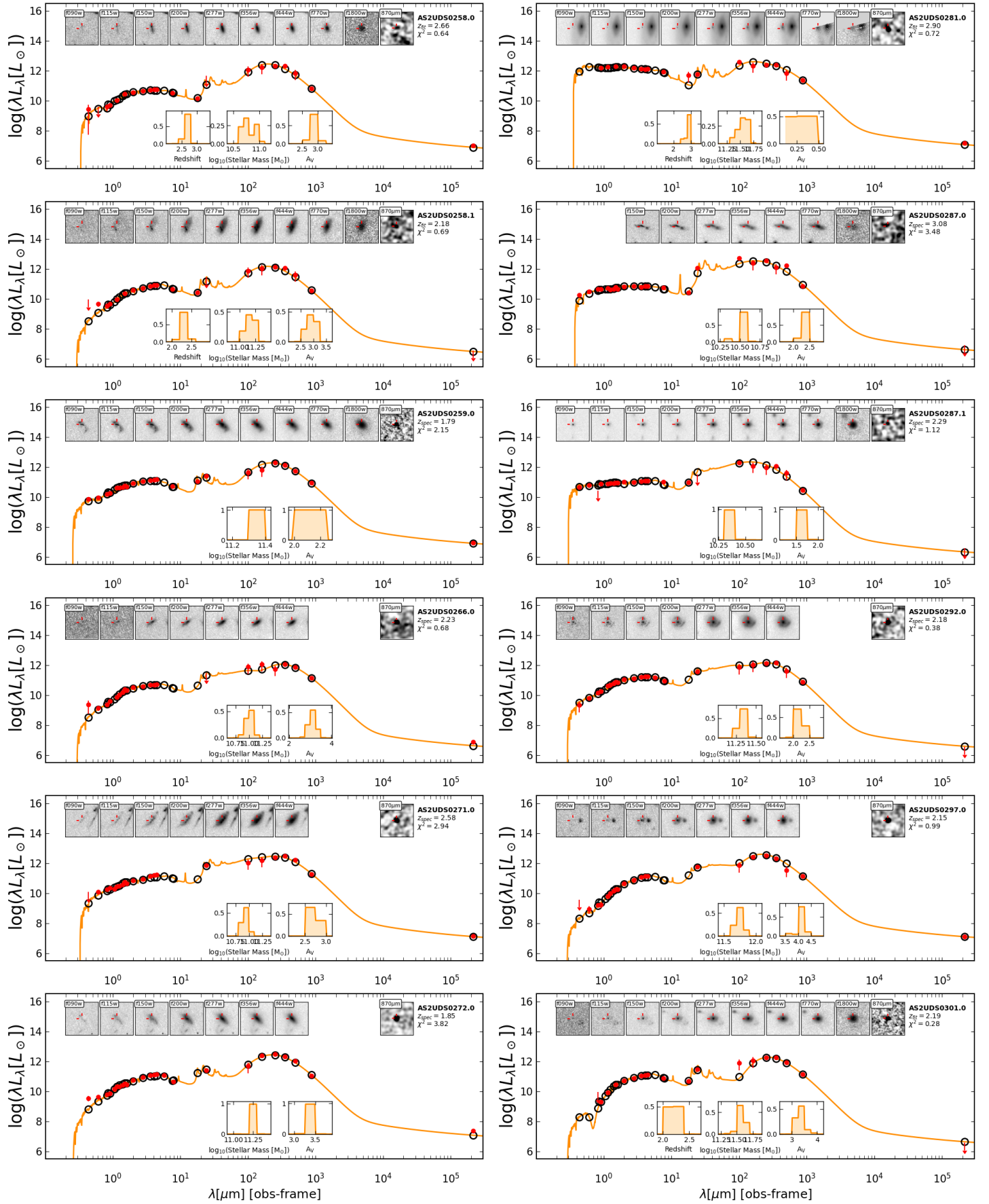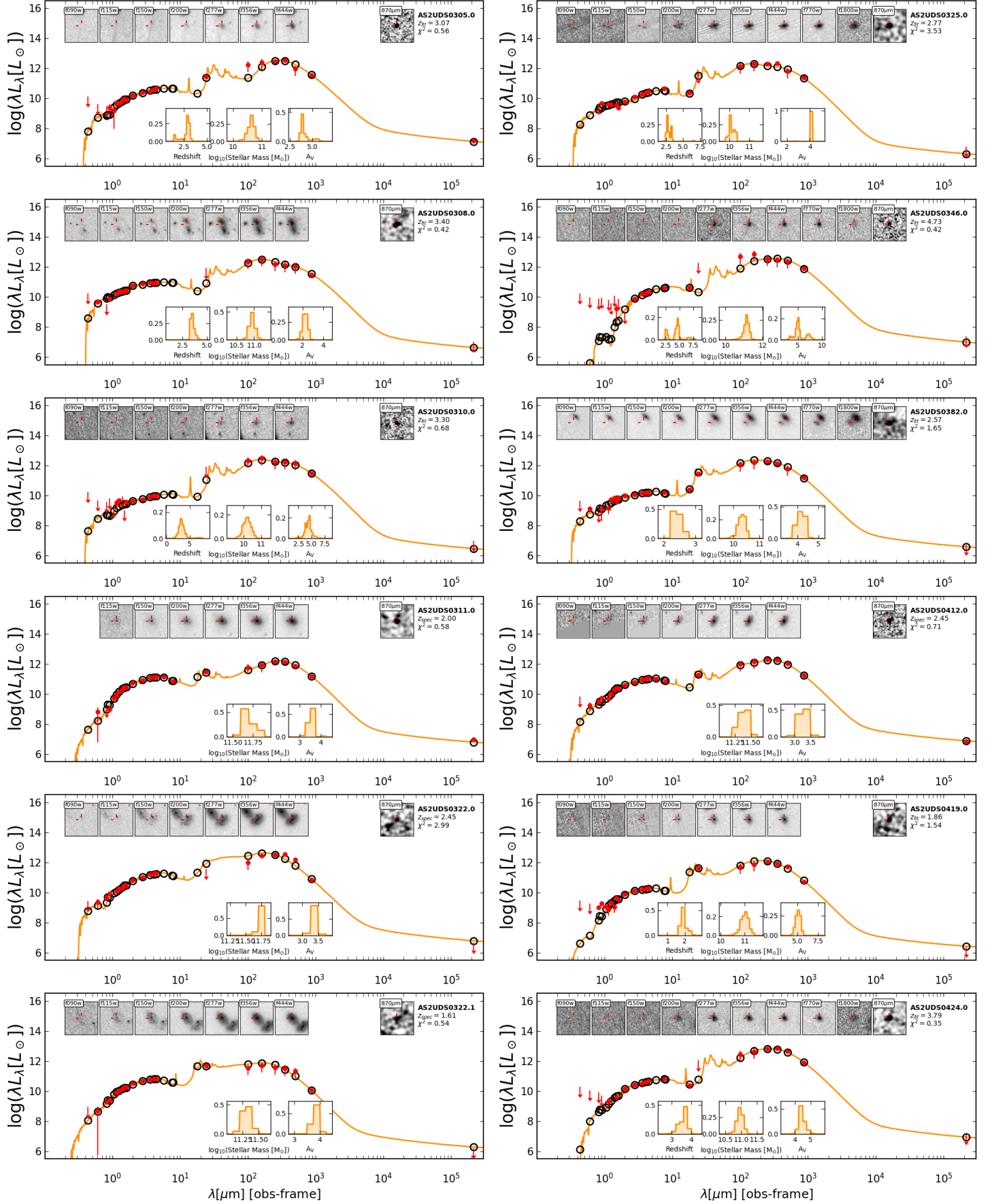
Fig. .2: Continued....

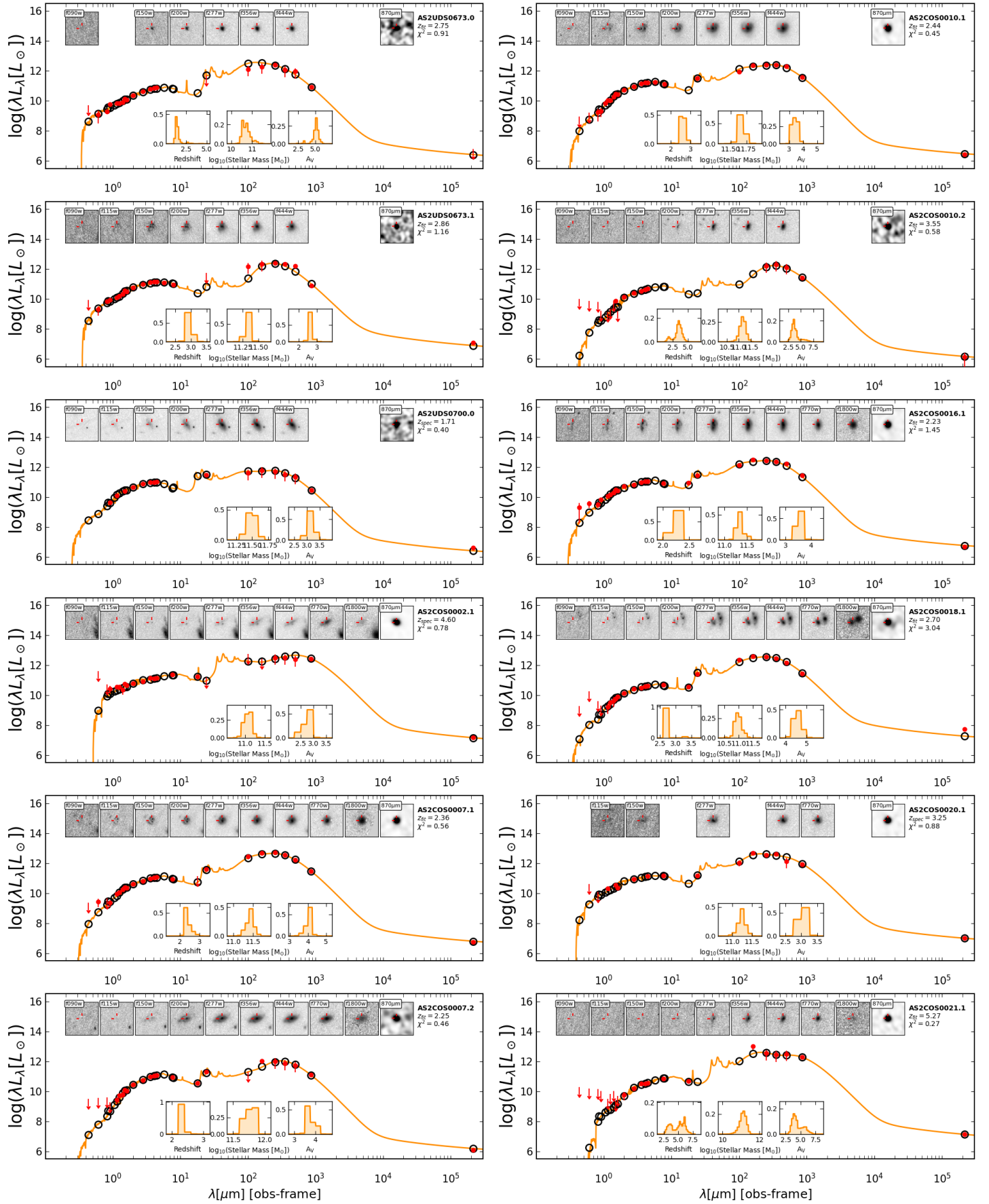Fig. .3: Continued....

Fig. .4: Continued....
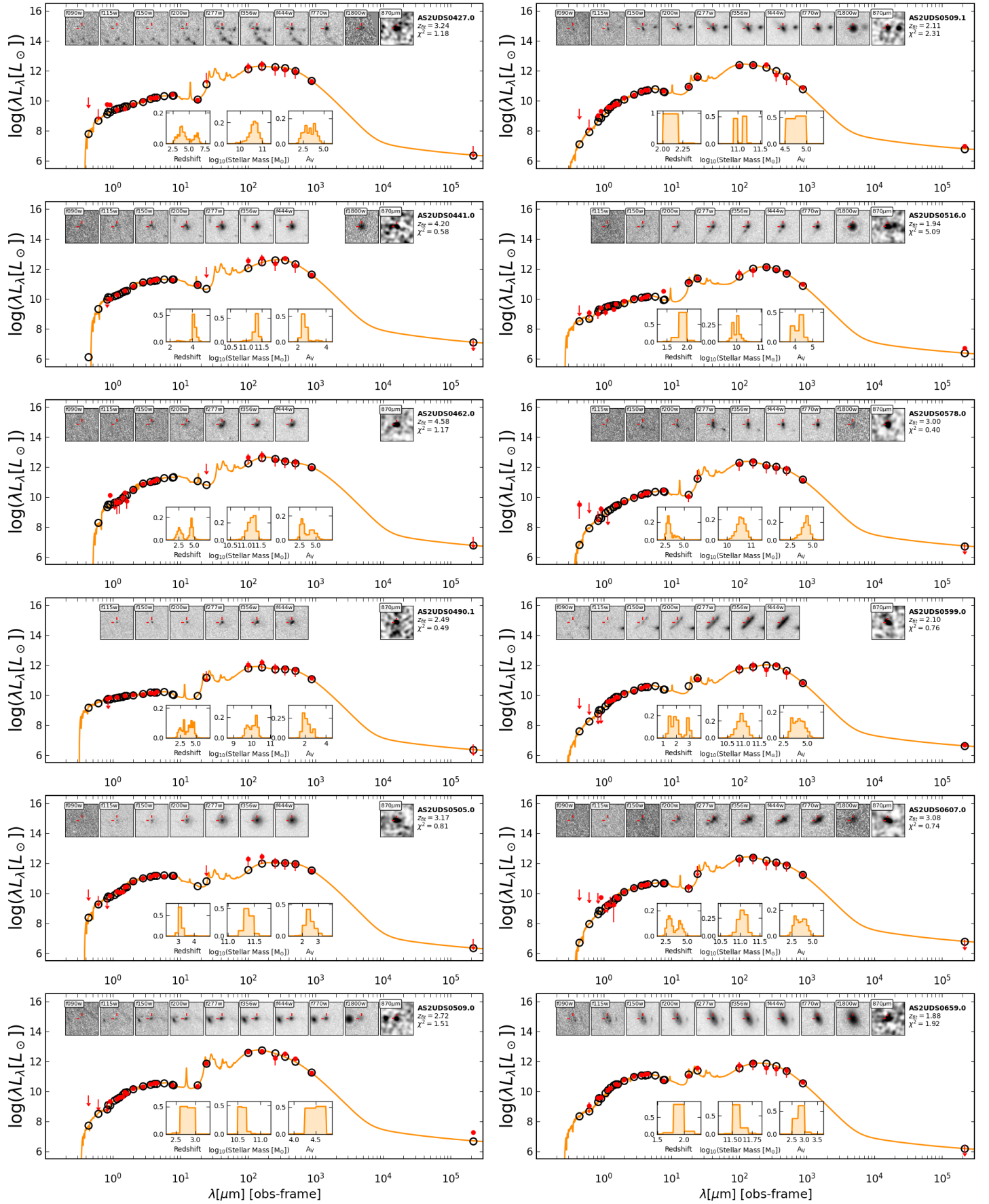
Fig. .5: Continued....

Fig. .6: Continued....
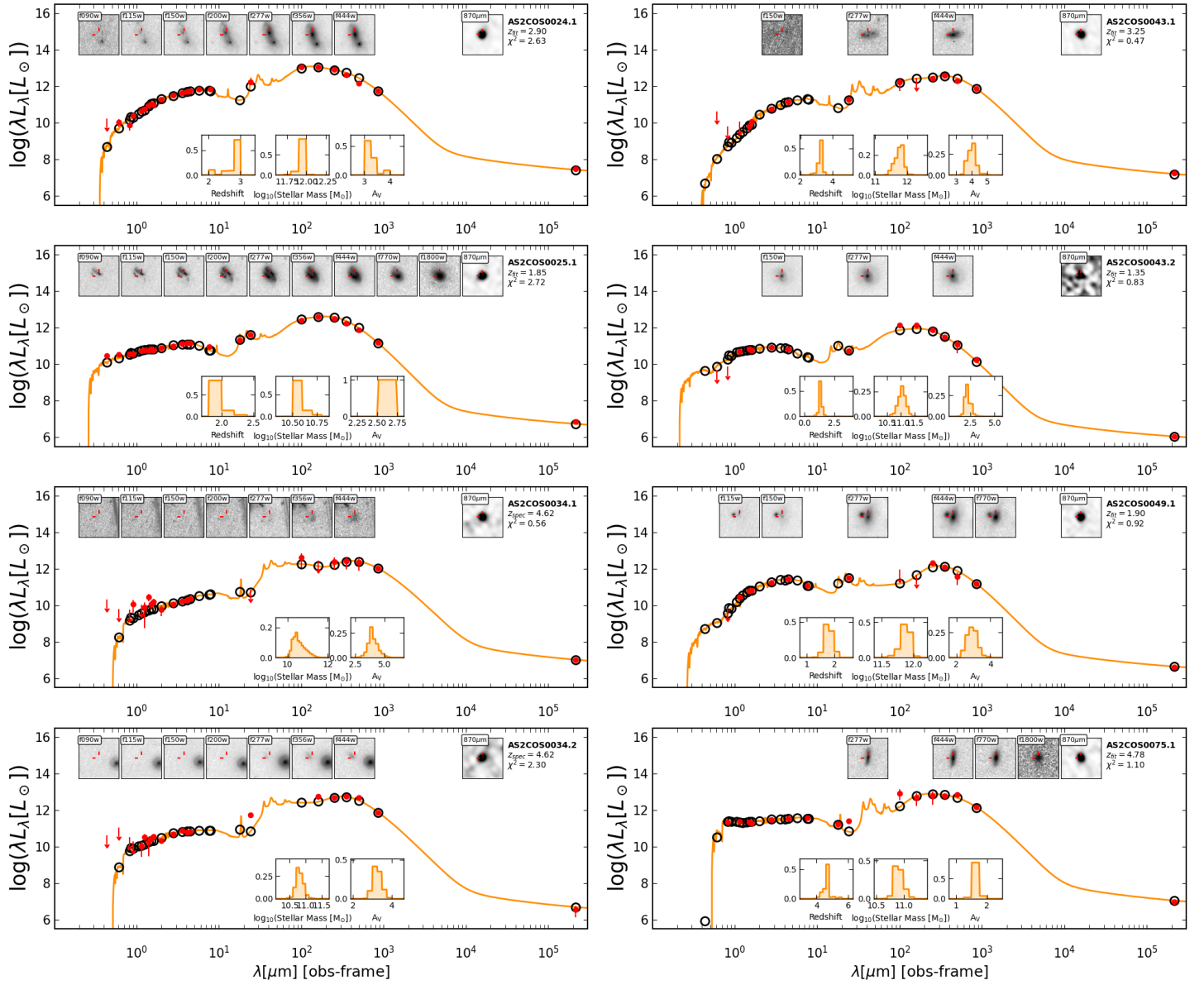
Fig. .7: Continued....

Appendix C: Rest-Frame Near-Infrared Sizes
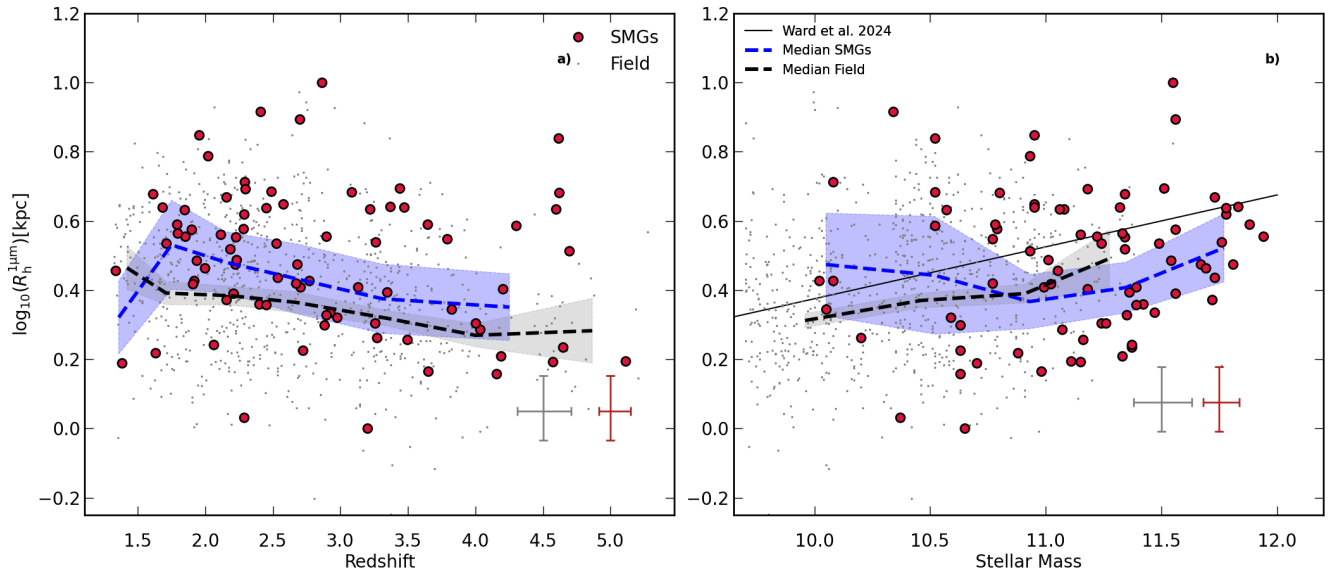

Fig. .8: The rest-frame 1μm half-light radius for SMGs (*red circles*) and field galaxies (*grey dots*) as a function of redshift (*a*) and stellar mass (*b*). In each panel, we show a running median for SMGs (dashed blue line) and field galaxies (black dashed line) as well as a representative uncertainty. We identify a consistent reduction in rest-frame 1μm size with increasing redshift in both field and SMG sample, as well as a consistent mass size relation to Figure 6. This indicates the morphology variation with wavelength identified in both samples in Figure 7 is not driven by redshift.